PALACKÝ UNIVERSITY OLOMOUC

FACULTY OF SCIENCE

DEPARTMENT OF PHYSICAL CHEMISTRY

CONVERSION OF CO$_2$ ON NANOSTRUCTURED CATALYSTS

MASTER'S THESIS

Author:	Bc. Karolína Simkovičová
Supervisor:	prof. RNDr. Libor Kvítek, CSc.
Study programme:	N1407 Chemistry
Specialization:	Material Chemistry
Form of study:	Full-time

Olomouc 2021

I declare that I have prepared this diploma thesis entitled "Conversion of CO_2 on nanostructured catalysts" independently under the guidance of doc. RNDr. Libor Kvítek, CSc. and RNDr. Štefan Vajda, CSc., Dr. habil. All literary sources and information sources used to prepare this work are listed in the bibliography, which is part of this work. I agree with the publication of the bachelor's thesis according to Act No. 111/1998 Coll. on Higher Education Institutions.

Signed 18. 5. 2021 in Olomouc,

………………………………..

Bc. Karolína Simkovičová

Acknowledgements

Bibliographical identification

Author:	Bc. Karolína Simkovičová
Title:	Conversion of CO_2 on Nanostructured Catalysts
Type of thesis:	Master
Department:	Department of Physical Chemistry
Supervisor:	prof. RNDr. Libor Kvítek, CSc.
Consultant:	RNDr. Štefan Vajda, CSc., Dr. habil.
Year of presentation:	2021

Abstract: The aim of this thesis was to study gas-phase catalytic hydrogenation of CO_2. The reaction mixture used contained CO_2, H_2 and He in the ratio of 1:5:4, with a total flow of 25 mL/min at a pressure of 1 bar. Catalysts were prepared using a 2-step synthesis of iron oxide and following the wet impregnation method of Cu NPs, with an increasing final load of Cu: 0%, 1%, 3% and 5%. All catalysts give methane as the main product, with C_2-C_4 paraffins, C_2-C_4 olefins, C_5^+ hydrocarbons and CO as additional products. Catalytic activity for each catalyst is slightly different, it follows a certain trend at each temperature, especially in the second temperature ramp, where the catalysts are in their final form of a mixture of iron oxides and iron carbides.

Keywords:	heterogeneous catalysis, CO_2 hydrogenation, conversion of CO_2 oxidative dehydrogenation, methane, iron oxides, copper nanoparticles
Number of pages:	73
Language:	English

Bibliografická identifikace

Autor:	Bc. Karolína Simkovičová
Název práce:	Konverze CO_2 na nanostrukturovaných katalyzátorech
Typ práce:	Magisterská
Pracoviště:	Katedra fyzikální chemie
Vedoucí práce:	prof. RNDr. Libor Kvítek, CSc.
Konzultant:	RNDr. Štefan Vajda, CSc., Dr. habil.
Rok obhajoby:	2021

Abstrakt: Cílem této práce bylo studium katalytické hydrogenace CO_2 v plynné fázi. Použitá reakční směs obsahovala CO_2, H_2 a He v poměru 1:5:4, s celkovým průtokem 25 ml/min při tlaku 1 bar. Katalyzátory byly připraveny pomocí dvoustupňové syntézy oxidu železa a metodou impregnace Cu NP v roztoku, se zvyšujícím se konečným obsahem Cu: 0%, 1%, 3% a 5%. Všechny katalyzátory poskytují jako hlavní produkt metan, přičemž jako další produkty jsou parafiny C_2-C_4, olefiny C_2-C_4, uhlovodíky C_5^+ a CO. Katalytická aktivita pro každý katalyzátor je mírně odlišná, sleduje trend při určité teplotě, zejména ve druhé teplotní rampě, kde jsou katalyzátory ve své konečné formě směsi oxidů železa a karbidů železa.

Klíčová slova:	heterogenní katalýza, hydrogenace CO_2, konverze CO_2, oxidativní dehydrogenace, methan, oxidy železa, nanočástice mědi
Počet stran:	73
Jazyk:	Anglický

Table of contents

1. Introduction

Ever since the industrial revolution, human activity has been emitting massive amounts of CO_2 into the atmosphere by burning fossil fuels. For the last two decades, the annual emissions of CO_2 increased to nearly 37 billion tons.[1] This of course creates a major challenge for modern science due to its contribution to global warming via the greenhouse effect.[2] One of the topics of modern science is CO_2 capture and/or its conversion to hydrocarbons [3, 4], which can be utilized as energy sources or precursors in the chemical industry. In particular, CO_2 can be used as a C_1 feedstock in many organic reactions, catalytically converting CO_2 into alcohols (methanol), hydrocarbons like methane, ethane or benzene, CO or carbonates and even derivates of hydrocarbons (e.g., carboxylic acids, aldehydes, amides and esters) [5-10].

The topic of CO_2 hydrogenation has been researched intensively for the last decades, however, there is still plenty of room to develop new routes towards high conversion and selectivity. Currently, the process in which CO_2 and H_2 are thermally activated on the catalytic surface, resulting in the formation of hydrocarbons, seem to be extremely interesting for industrial implementation. During this reaction, CO_2 and H_2 are transformed into CO and water – a process known as reverse water gas shift (RWGS). CO can then enter a reaction with excess H_2, the well documented Fischer-Tropsch (FT) synthesis.[11] Therefore, catalysts for CO_2 hydrogenation must be active in both RWGS and TS, which are slightly endothermic and exothermic, respectively.[12-15] As a result, higher CO_2 conversion can only be accomplished if the FT route is effective in overcoming the RWGS thermodynamic constraint.[16]

The production of higher hydrocarbons is influenced by the balance between RWGS and FT processes. Preparation of multifunctional catalysts can solve this problem and, in this work, Cu/FeO_x catalyst that takes advantage of both Cu and FeO_x's inherent abilities are studied, with Cu serving as the RWGS catalyst and FeO_x selectively yielding C_2-C_4 olefins by FT from its in situ generated Fe_5O_2, with the result of different copper contents studied. The combination of Cu and Fe catalysts have already been reported with selectivity to higher hydrocarbons.[17, 18]

2. Theoretical part

2.1. Catalysis

Catalysis is a process of increasing the rate of a chemical reaction and altering the reaction mechanism by adding a catalyst, without modifying the overall standard Gibbs energy change in the reaction.[19] The catalyst is a reactant as well as a reaction product, meaning that it exits the reaction chemically unaltered.[20, 21] Catalysts can increase the rate of a chemical reaction (positive catalysis) or decrease it (negative catalysis, inhibition) but strictly speaking, „catalyst" is used only for positive catalysts.[22] The principle of the catalyst function is to reduce the activation energy (Gibbs energy) of the reaction by changing the reaction pathway.[21, 22] Uncatalyzed and catalysed reaction coordinates are shown in Figure 1.
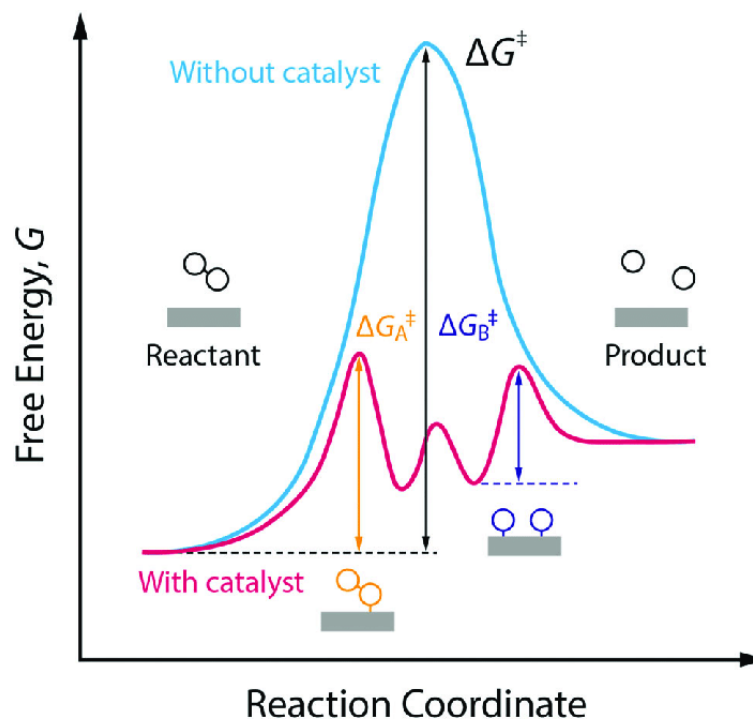
Figure 1. Reaction coordinate diagram showing the working principle of a catalyst.[23] $\Delta G^{\ddagger}$ is the activation energy of an uncatalyzed (catalysed) reaction.

The primary classification of catalytic reactions is based on the system's phase composition. Homogeneous catalysis occurs when the catalyst is in the same phase as the reaction mixture. Catalysis is heterogeneous when the catalyst is in a different phase than the reaction mixture.[21, 22, 24]

In contrast to all other kinds of catalysis, the catalyst in autocatalysis is a result of the total process. The hydrolysis of an ester, such as aspirin, to carboxylic acid and alcohol, is an example. In the absence of additional acid catalysts, the hydrolysis is catalysed by the carboxylic acid product.[24]

Enzyme catalysis, in which the enzyme functions as a biocatalyst, is a unique example. For enzyme catalysis, many reaction mechanisms can be identified, the simplest and best known of which is the Michaelis-Menten mechanism.[24]

2.1.1. Heterogeneous catalysis

Heterogeneous catalysis is specific catalysis, it has an advantage in that the catalyst prefers a certain reaction route out of many other possible ones, for example with the formation of isomers. Much purer products are formed during heterogeneous catalysis. Another advantage is relatively easy separating the solid catalyst from the gaseous/liquid reactants and products and easier regeneration of the catalyst. However, in actuality, catalysts do not have an indefinite service life. Changes in the catalyst's structure or the products of side reactions cause the catalyst to deactivate.[21, 22, 24]

Heterogeneous catalysis takes place in active sites on the surface of the solid material (catalyst). Catalysts are generally materials with a large surface area (10-1000 $m^2.g^{-1}$)[25], and therefore with a high number of active sites per unit volume (or mass) of catalyst. Large surface areas of a substance are attained by shrinking its dimensions, which is why the majority of catalysts used in practice are micrometre-sized particles or porous materials.[22]

The surface structure of crystalline catalysts varies greatly from the interior structure (Figure 2). The absence of binding interactions between atoms on the surface and interior atoms leads to an increase in surface energy. The surface structure changes as a result of this scenario, and the atoms reorganize in a more energy-efficient manner. Furthermore, with the adsorbed atoms, a chemical link is created (chemisorption). Surface defects that occur on individual terraces that separate stairs, where there may be additional defects induced by bending, have a substantial impact on catalytic processes. On these terraces are adsorbed atoms (called adatoms) and also some vacancies can appear here.[26]
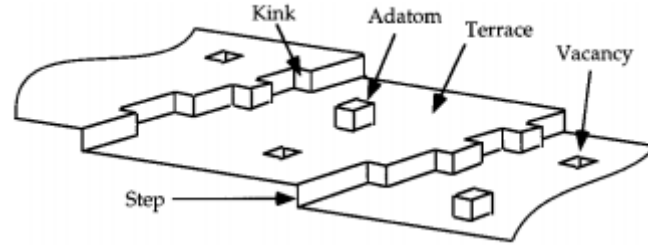
Figure 2. A simple model of defects on a crystal surface.[26]

In the case of heterogeneous catalysis, the catalytic reaction is a complex sequence of processes. Firstly, reactants are transported to the surface of the catalyst particles by diffusion. Then, reactants are adsorbed to active sites. Reactions take place on the surface of the catalyst in which various intermediates are formed or converted. The products are desorbed from the catalysis site and transported to the surface of catalyst particles (diffusion).[22]

The kinetic equation for catalytic history is individually expressed only for the governing history, usually by the slowest. The controlling process is also a chemical reaction, but can often be a controlling process as well as an adsorption reactant or, conversely, a desorption product. The kinetic equation of the reaction on the catalyst surface can be expressed by Equation 1, where θ_i is the surface concentration of substance i, τ is the adsorption time, k_A is the rate constant of the direct reaction and k_B of the opposite reaction.

$$-\frac{d\theta_A}{d\tau} = k_A\theta_A - k_B\theta_B \tag{1}$$

The surface concentration can be expressed from the Langmuir isotherm, which describes single-layer adsorption at a homogeneous surface of the adsorbent and a mutual non-influence of the adsorbate molecules. The Langmuir isotherm can be expressed by Equation 2, where a_{max} is the amount of adsorbed gas needed to completely cover the surface with a monolayer at equilibrium pressure $p \rightarrow \infty$, a is the amount of gas adsorbed at equilibrium pressure and b is only a function of temperature.[27]

$$\theta = \frac{a}{a_{max}} = \frac{b.p}{1 + b.p} \tag{2}$$

By combining equations (1) and (2), considering several possibilities in terms of the interaction of the catalyst surface with the reactants and products, a kinetic equation for the respective catalytic process can be obtained. The best known is probably the mechanism according to Langmuir and Hinshelwood when the adsorption of substances A and B on active sites is strong enough. For the rate of the reaction applies Equation 3 where the product R also participates in the sorption equilibrium, occupying a part of the catalyst surface (θ_R).[22]

$$v = k.\,\theta_A.\,\theta_B = k.\frac{K_A K_B p_A p_B}{(1 + K_A p_A + K_B p_B + K_R p_R)^2} \tag{3}$$

Adsorption is significantly affected by the occurrence of defects on the surfaces, and thus by a change in the electronic structure. The reactivity of atoms is thus different in different positions, which is a very important factor for catalytic reactions. Adsorption depends on the physical properties of the adsorbate in terms of atoms, ions, molecules, groups of molecules, and their size, shape, mass, but also chemical properties.[22]

In heterogeneous catalytic reactions, the temperature has a significant effect. Temperature affects the rate constant, which increases with increasing temperature. This phenomenon can be expressed by the Arrhenius equation (Equation 4). With increasing temperature, the adsorption coefficient decreases, meaning the decrease of reactants and products concentration on the catalyst surface, which can be expressed by Equation 5. *k* is the rate constant, *A* is the Arrhenius constant, λ is the heat of absorption, E_A is the activation energy of the chemical reaction, *R* is the molar gas constant, *T* is the thermodynamic temperature.[22]
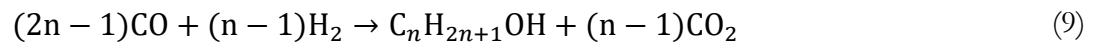
$$k = A.\,e^{-\frac{E_A}{RT}} \tag{4}$$

$$k = K_0.\,e^{\frac{\lambda}{RT}} \tag{5}$$

2.1.2.   Fischer-Tropsch synthesis

One method for producing liquid transportation fuels from carbon-containing feedstocks is Fischer-Tropsch (FT) synthesis. FT synthesis was formerly primarily utilized to convert coal or natural gas to diesel and gasoline. The principle of FT is the conversion of raw carbon materials (i.e. natural gas, oil residues, biomass or coal) into more usable intermediates and fuels.[11, 28, 29]

FT synthesis is a difficult process, and the actual mechanism of FT synthesis remains unknown to this day. Some reactions occurring are listed in the following equations (Equations 6-9). C_1-C_{60} are then processed to motor fuels, however, not all products that can arise from FT are suitable for further processing.[11, 28, 29]

$$nCO + (2n + 1)H_2 \rightarrow C_nH_{2n+2} + nH_2O \tag{6}$$

$$nCO + 2nH_2 \rightarrow C_nH_{2n} + H_2O \tag{7}$$

$$nCO + 2nH_2 \rightarrow C_nH_{2n+1}OH + (n - 1)H_2O \tag{8}$$

$$(2n - 1)CO + (n - 1)H_2 \rightarrow C_nH_{2n+1}OH + (n - 1)CO_2 \tag{9}$$
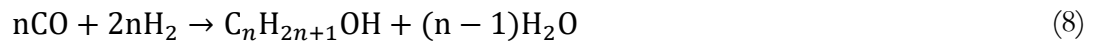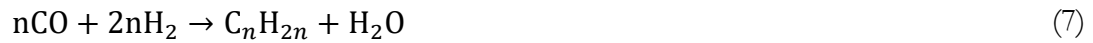
2.2. Catalytic hydrogenation of CO_2

Human activity has been releasing large volumes of CO_2 into the atmosphere by burning fossil fuels since the industrial revolution. CO_2 emissions have climbed to approximately 37 billion tons per year over the last two decades.[1] To this date, the levels of CO_2 in our atmosphere reached over 415 ppm[30] (Figure 3). The result of burning fossil fuels is its contribution to global warming, by increased production of "anthropogenic" greenhouse gases, thanks to their ability to absorb and re-emit infrared radiation.[2, 31, 32] The most abundant greenhouse gases are CO_2, next is methane, N_2O, SF_6 and fluorocarbons. One of the ways to prevent this trend, mitigate the impact of the greenhouse effect and improve the climatic conditions on Earth, is to reduce the concentration of CO_2 in the atmosphere by its further use.
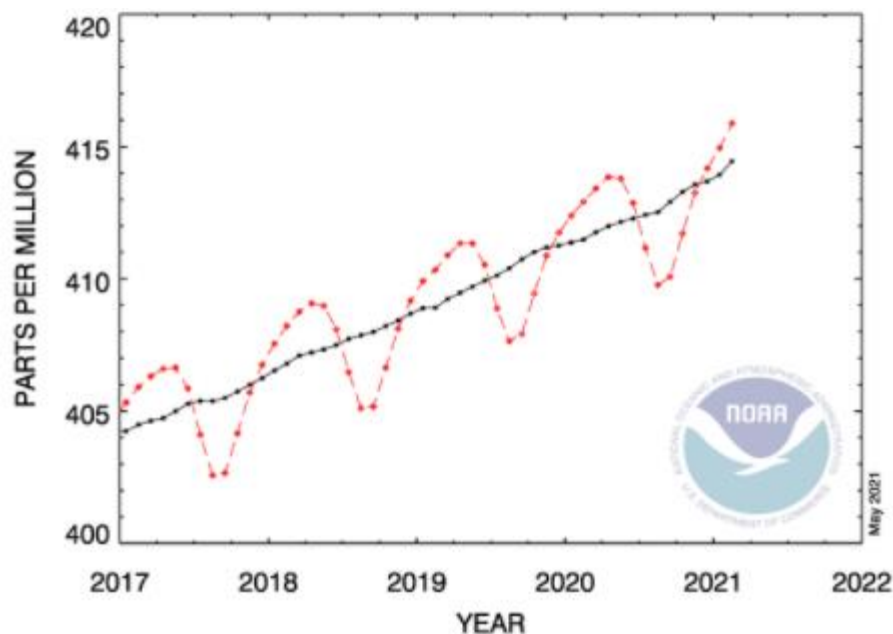
Figure 3. Recent global monthly mean CO_2 in the atmosphere.[30]

CO_2 collection and conversion to hydrocarbons which may be used as energy sources or precursors in the chemical industry are one of the topics of interest in modern science.[3, 4] CO_2 can have a direct (physical) application, for example in the food industry to make decaffeinated coffee by removing the caffeine from coffee beans and for carbonating beers and soft drinks. Other uses of CO_2 are dry ice, solvent, refrigerant, for welding or fire extinguishers. However, the direct use of CO_2 is low due to its production as waste and thus has an overall insignificant effect on reducing the concentration of CO_2 in the atmosphere.

As mentioned previously, CO_2 is the starting material for the production of energy-relevant substances by hydrogenation of CO_2 such as carbon monoxide, hydrocarbons (methane, etc.), alcohols (methanol, etc.). In addition to hydrogenation, CO_2 is suitable for the production of epoxides by a cycloaddition reaction, carbonylation of amines or alcohols, copolymerization of CO_2 with organic molecules and derivates of hydrocarbons (carboxylic acids, aldehydes, amides and esters).[5-10] Methanol, dimethyl ether and dimethyl carbonate appear to be the most important energy products that could replace fossil fuels in the future.[33]

Carbon dioxide is a non-polar molecule that comprises two polar C-O bonds and 16 valence electrons. CO_2 has two potential reaction sites: the carbon atom is electrophilic, while the oxygen atoms are nucleophilic, allowing the CO_2 molecule to be activated or converted into various chemicals. An active catalyst and effective reaction conditions are needed for the conversion of CO_2 into useful chemicals. Thus, the reaction of CO_2 with substances that have a higher free Gibbs energy than CO_2 (eg. H_2 or CH_4) is used, which results from the thermodynamics of CO_2 conversion.[34]

The surface chemistry and catalysis challenge in CO_2 hydrogenation is to figure out how to synthesize a metal oxide catalyst with the best mix of surface properties and long-term stability to favour the synthesis of one specific carbon dioxide hydrogenation product at the highest feasible conversion rate and without interference from products like CO or H_2O. Deactivation by sintering or poisoning is also one great challenge.

While this task may appear overwhelming at first, decades of research into oxide defect characteristics, as well as recent breakthroughs in synthetic, characterization, and computational approaches, have made a rational design of high-performance, defect mediated metal oxide heterogeneous catalysts for CO_2 fixation a reality.

2.2.1. Mechanism of CO_2 hydrogenation

Metal oxides are the most common materials that demonstrate activity in the catalytic hydrogenation of CO_2 to energy-relevant compounds. Metals make up a substantial section of the periodic table, but their utility isn't limited to their abundance, stability, low cost, or capacity to be nanostructured. The ability to check for faults in the structure of metals is the most crucial. The most crucial is the ability to inspect metals for structural defects that affect their qualities, function, and applications.[35]

The mechanism of CO_2 hydrogenation and strength of adsorption depends on the elemental composition of the metal oxide and its structure and defects. The interactions occurring can range from the weak physical to the strong chemical.[35, 36] CO_2 can be adsorbed on the surface of the metal oxide (MO_x) by coordination to one or two adjoining metal atoms through oxygen atoms of the CO_2. CO_2 can also be coordinated through the carbon atom to the surface oxygen atom of the MO_x. Surface oxygen vacancies can operate as extra adsorption sites in non-stoichiometric $MO_x[O]_z$ by interacting with the carbon and/or oxygen atoms of CO_2. In nonstoichiometric $MO_x[M]_z$, the surface metal vacancies can also act as CO_2 adsorption sites. In the case of hydroxides MO_xOH_y or $MO_xOH_y[O]_z$, CO_2 can bind to the surface, for example as carbonates or bicarbonates.[35] All mentioned mechanisms are illustrated in Figure 4.
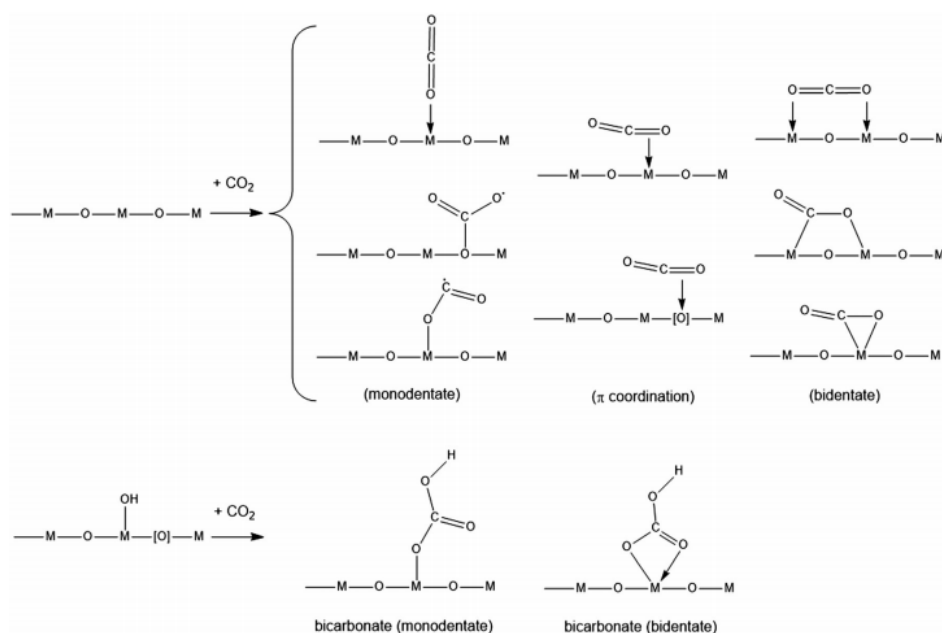
Figure 4. Possible mechanisms for adsorption of CO_2 on the surface of the metal oxide catalysts.[35]

Metal oxides, both stoichiometric and non-stoichiometric, have been shown to split molecular H_2 heterolytically into a proton and hydride sites, and homolytically into two proton sites, as shown in Figure 5. This capacity opens up a lot of possibilities for adjusting the adsorption, reactivity, and selectivity behaviour of metal oxides for the hydrogenation of CO2 into fuels. Surface bound bicarbonate, formate, carbide, carbonyl, and methoxy groups are possible reaction intermediates in heterogeneous catalytic hydrogenation of carbon dioxide (Figure 6).[35]

The intermediates further react and desorb as products of the catalytic hydrogenation of CO_2, which may be formic acid, formaldehyde, methanol, carbon monoxide and methane.[36]
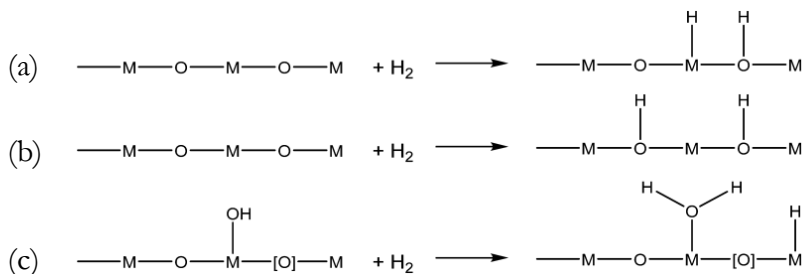
Figure 5. Different mechanisms of activation of H_2 by metal oxide catalysts: (a) heterolytic, (b) homolytic and (c) heterolytic dissociation of H_2.[35]
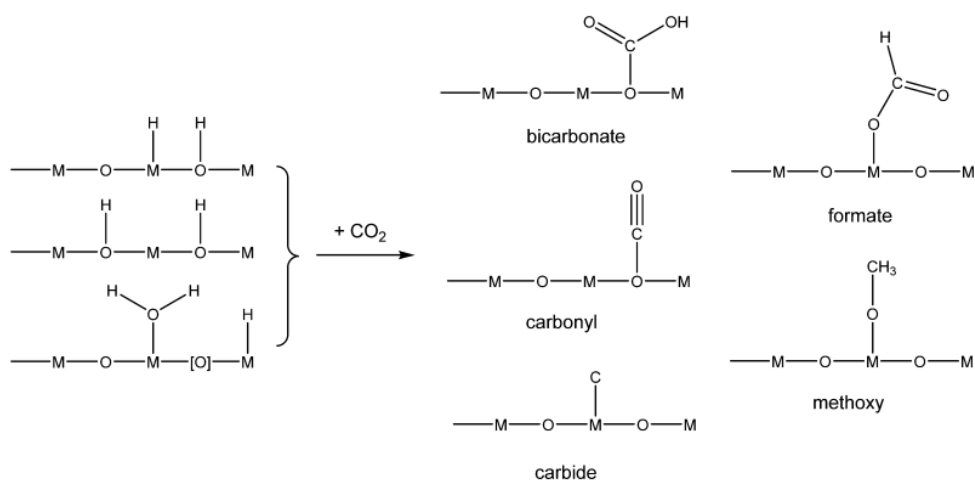
Figure 6. Possible products of catalytic hydrogenation of CO_2.[35]

2.2.2. Expected products

The most common products of CO_2 hydrogenation are methane, methanol and synthetic gas (syngas) and these can be expected products when studying the catalytic properties of certain metals or metal oxides.

Methane is a major component of natural gas and a major source of C_1 carbon. Hydrogenation of CO_2 and CO to form CH_4 and water proceeds according to the following equations (Equations 10, 11).[32] Both CO_2 and CH_4 are relatively cheap gases due to their

occurrence in nature. CH_4 is catalytically converted to synthesis gas, which is used for further conversion to more energy-efficient products.[37]

$$CO_2 + 4H_2 \rightarrow CH_4 + 2H_2O \qquad\qquad \Delta H^0{}_{298} = -164.7 \text{ kJ/mol} \qquad (10)$$

$$CO + 3H_2 \rightarrow CH_4 + H_2O \qquad\qquad \Delta H^0{}_{298} = -206 \text{ kJ/mol} \qquad (11)$$

The synthesis of gas, which contains mostly methane, is now one of the most sophisticated technologies known as Power-to-Gas. It's a reaction of H_2 and CO_2 that produces a gas with a high CH_4 content, known as synthetic natural gas (SNG). The Sabatier reaction, which operates according to Equation 11, also produces CH_4, the requisite H_2 is supplied by water electrolysis. Natural gas is used in the chemical industry mainly as a starting material for the production of synthesis gas (mixture of CO and H_2) by the steam-methane reforming method. At 250° C, the Sabatier reaction produces the maximum yield. Water, H_2, and CO_2 are also present in the resulting SNG. This SNG may be supplied into the natural gas network after the water has been removed and used for heating.[38]

Syngas (a mixture of H_2 and CO) is traditionally produced by the oxidation of raw carbon materials such as natural gas, petroleum residues, biomass or coal. Syngas is further processed into more valuable chemicals and fuels by FT.[29] CO_2 can also be used to produce synthesis gas by reaction with methane (Equation 12).[37] There are several technologies, the choice of which then affects the final composition of the products. The most commonly used technologies are steam-methane reforming, dry-methane reforming, auto-thermal reforming and partial oxidation. The conversion of CO_2 yields synthesis gas with an H_2:CO ratio of 2:1, which is ideal for FT, water is frequently a by-product.[32] Some catalysts were studied for conversion of CO_2 to CO by reverse water gas shift (RWGS), according to Equation 13.[39, 40]

$$CO_2 + CH_4 \rightarrow 2CO + 2H_2 \qquad\qquad \Delta H^0{}_{298} = 247.3 \text{ kJ/mol} \qquad (12)$$

$$CO_2 + H_2 \rightarrow CO + H_2O \qquad\qquad \Delta H^0{}_{298} = 42 \text{ kJ/mol} \qquad (13)$$

The next most desired product is methanol. Methanol is used in medicine, pharmacy, dyes, plastics, etc. Methanol is also the starting material for the production of dimethyl ether and dimethyl carbonate, other energetically important compounds. It is industrially produced by the conversion (Equation 14) of synthesis gas using Cu-Zn catalyst at 5-10 MPa and 200-300°C. Recently, research has focused more on the production of methanol from CO_2

(Equation 15).[34] However, this is a major challenge due to the high activation energy of CO2, and the reaction may be accompanied by RWGS (Equation 13).

$$CO + 2H_2 \rightarrow CH_3OH \qquad\qquad \Delta H^0{}_{298} = -91 \text{ kJ/mol} \qquad\qquad (14)$$

$$CO_2 + 3H_2 \rightarrow CH_3OH + H_2O \qquad\qquad \Delta H^0{}_{298} = -49 \text{ kJ/mol} \qquad\qquad (15)$$

Because the synthesis of methanol is an exothermic process, whereas the feedback reaction is endothermic, thermodynamics predicts that the amount of methanol created rises as the temperature decreases. However, due to its inert qualities and limited reactivity, CO_2 may be activated to make methanol up to a temperature of 240°C. At high temperatures, however, the synthesis of by-products such as other alcohols and hydrocarbons is favoured, reducing selectivity.

2.2.3. Catalysts for CO_2 hydrogenation

Several Ru, Ir, Fe, Mn, Ni and Co-based catalysts[12, 41-59], have been identified for CO_2 conversion to higher hydrocarbons but discovering catalysts that are highly selective to obtain desired products remains a major challenge.

CO_2 hydrogenation produces more low molecular weight hydrocarbons rather than $C_5{}^+$ materials, which are more useful as liquid transportation fuels since CO is the chain increasing agent in FT reaction.[11] When utilizing CO and H_2 (synthetic gas, syngas) to produce long-chain hydrocarbon, cobalt-based catalysts are very active, but when switching to CO_2 and H_2 mixture, they only generate methane.[60, 61]

Catalysts In_2O_3 a Ga_2O_3 have been studied for their activity in RWGS, with CO_2 conversion using In_2O_3 reaching up to 35%[62]. Regarding the production of syngas, Rh based catalyst demonstrated over 77% conversion of CO_2 to CO[63]. Bimetallic catalysts - Co-Fe[64], Ru-Co_3O_4[65], Ni-Ga[66] or Co-Pt/TiO_2[60] – display a very high selectivity towards the production of methane in CO_2 hydrogenation. Overall, Ir and Ru based catalysts are highly active in CO_2 hydrogenation, but they produce methane nearly exclusively.[67, 68]

Iron is one of the most studied metals for FT and CO_2 hydrogenation, as it can adsorb and activate CO_2[69], which is a determining factor for direct CO_2 conversion to short-chain olefins due to its intrinsic RWGS and FT activity. Using alkali metals as promotors of Fe catalysts for CO_2 conversion to light olefins was reported in several papers, but they require

temperatures over 300°C and pre-treatment under hydrogen or CO atmosphere for over 12 hours.[43, 70-78]

Fe catalysts with Cu promoters have also been reported but yielded low selectivity for light olefins and high for methane. [79, 80] If we focus on Cu based catalysts, many reported its high selectivity towards methanol[81-90] with the effect of copper (nanoparticles or clusters) active surface area to methanol selectivity[91]. Copper tetramers (Cu_4) were investigated for their high efficiency in the production of methanol as well.[92]

Selectivity for higher hydrocarbons has already been demonstrated using a Cu and Fe catalyst combination, which takes advantage of both Cu and FeO_x's attributes. Cu serves as the RWGS catalyst, and FeO_x preferentially yields C_2-C_4 olefins via FT from its *in-situ* created Fe_5O_2, with various copper concentrations examined. [17, 18, 93-95]
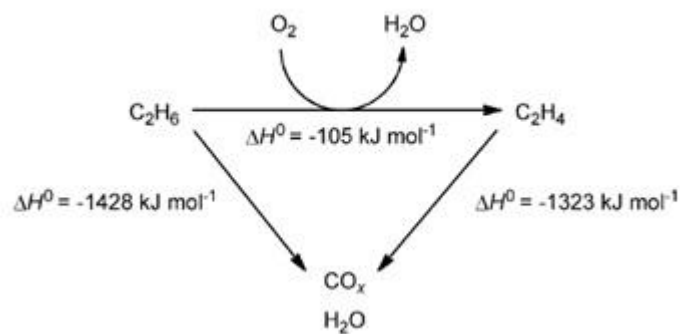
2.3. Oxidative dehydrogenation

Light olefins, mainly ethylene and propylene [96], are some of the most desirable compounds in the chemical industry because they can be used in the synthesis of a wide range of chemicals, including polymers. With the increasing demand for these compounds connected with increasing population and rising living standards, the production of them is likely to increase.

The current most used technology for olefin production is steam cracking (SC)[97]. The typical precursors for SC are naphtha and components of natural gas. There are many types of this process known, depending on the length of the carbon chain in the precursors. These techniques have however high demands for energy input and relatively have low selectivity for a particular olefin product. Not to mention that petroleum is not a renewable source. Because of that, there's been recently a strong interest for researchers to study oxidative dehydrogenation (ODH) of alkanes. Carbon dioxide can be recovered from the atmosphere and then used in ODH. It can be a source of carbon – as it was for the past decades, and only recently it has been proposed as a source of oxygen – or an oxidant for partial oxidation of light alkanes. It is expected to become an important route for the utilization of natural gas, which in many areas contains carbon dioxide and methane and other light olefins, into valuable chemicals of fuels.[98, 99]

As opposed to oxidative dehydrogenation, direct dehydrogenation of hydrocarbons can be used. This process is renewable, thanks to the hydrogen involved, and the hydrogen does not get oxidized to water, but it is a strongly endothermic reaction and there is an increased risk of unwanted side reactions that occur in those high temperatures (more than 600°C). On top of that, the catalyst is degraded much faster. Oxidative dehydrogenation of light alkanes has advantages compared to processes still implemented on a larger scale, such as high conversion rates and potentially lower reaction temperatures.[99] ODH of ethane is illustrated in Figure 7.

Currently in the commercial processes, mostly platinum and chromium oxides are used as catalysts, but also other metal oxides, such as gallium oxides, vanadium oxides, molybdenum oxides and indium oxides, are used.[100-113]

Figure 7. Oxidative dehydrogenation of ethane with side reaction.[99]

Copper is also a promising catalyst in ODH processes, in combination with other metals or with different supports or promoters.[101, 114-136] In 2005, Zaccheria *et al.* reported very high selectivity and high conversions with 8% wt. Cu/Al_2O_3 in the oxidation of aromatic secondary alcohols [136], without the need of adding any "poisoning agent" which would stop the formation of undesired products.

3. Experimental part

In this chapter, the preparation of the catalysts is described, via a two-step preparation of iron oxide and a wet impregnation of copper nanoparticles onto the surface of iron oxide. Then, the characterization of the prepared fresh catalysts and catalysts after the reaction is discussed. And lastly, their catalytic activity is studied on the catalytic hydrogenation of carbon dioxide. Four catalysts were prepared, with increasing total copper content, therefore, the emphasis in this work is on the influence of copper content on the conversion and selectivities towards products.

3.1. Chemicals

For the preparation of iron oxide precursor, the following chemicals were used: oxalic acid ($C_2H_2O_4$, ≥99%, Sigma-Aldrich), *N,N*-dimethylacetamide (C_4H_9NO, anhydrous, 99.8%, Sigma-Aldrich), iron (II) chloride ($FeCl_4$, 98%, Sigma-Aldrich). In the preparation of the final catalysts, copper sulphate pentahydrate ($CuSO_4.5H_2O$, ≥99%, Sigma-Aldrich) and hydrazine hydrate ($N_2H_4.H_2O$, reagent grade, Sigma-Aldrich) were used.

Deionised water (purity 0,05 µS·cm^{-1}, AQUAL 29, Merci) was used for the preparation of the solutions for the synthesis of the catalysts and for washing steps, in which also ethanol (95%, denatured with methanol, Thereons TTD, a. s.) was used.

The gases for CO_2 hydrogenation, CO_2 (99.99%), H_2 (99.99%) and He (99.99%), were purchased from Airgas.

3.2. Instrumentation

The preparation and subsequent characterization of the prepared catalysts were conducted using the following instruments and laboratory equipment. Sonicator SONOPULS HD 4400 Ultrasonic homogeniser and additionally, electromagnetic stirrer MR 1 000 from Heidolph Instruments were used for mixing the solution during synthesis. Eppendorf Centrifuge 5702 was used for the separation of the solid products from solvent. Catalysts were dried at room temperature in an inert nitrogen atmosphere in a glove box from GS Systemtechnik GmbH to avoid oxidisation of the catalysts before testing.

Microscopic images were procured using the following microscopes. Transmission electron microscopy (TEM) characterization was conducted with JEOL TEM-2100 multipurpose electron microscope equipped with an energy-dispersive X-ray spectroscope (EDX) for elemental mapping. The microscope is able to take images with 0.19 nm resolution and magnification of 1000-800 000x. For Scanning electron microscopy (SEM) analysis, HITACHI SU 6600 scanning electron microscope was used, with a resolution of 1.3 nm and magnification of 60-600 000x equipped with EDX for elemental mapping. High-Resolution Transmission Electron Microscope (HRTEM) FEI Titan 60-300 kV with resolution 0.14 nm was used for conducting scanning transmission electron microscopy with high-angle annular dark-field imaging (STEM/HAADF), equipped with EDX for elemental mapping. The microscope has a resolution of 0.14 nm

The phase composition of the catalysts was determined with powder X-ray diffraction (XRD) analysis, which was conducted with Malvern Panalytical Empyrean diffractometer.

The final content of copper in the catalysts was determined using atomic absorption spectroscopy (AAS), conducted on Analytic Jena AG ContrAA 300 spectrometer with flame ionization. Typically, a small, specific amount of the sample was dispersed in 100 ml deionized water, containing 5 ml of nitric acid (HNO_3) and sonicated for 10 minutes. The remaining solids were filtered off before analysis.

Sorption of gas was measured on surface area analyser Autosorb iQ-C-MP (Quantachrome Anton Paar), using ASiQWin software at 77 K up to the saturation pressure of N_2, and for calculating the specific surface area, Brunauer-Emmett-Teller (BET) model was used. The points for multi-point BET were determined using Roquerol's method, and are within the standard range of $p/p_0 = 0.05$ to 0.3. Before surface analysis, all catalysts were treated at 130°C for 12 h.

X-ray photoelectron spectroscopy (XPS) was conducted on PHI 5000 VersaProbe II spectrometer with monochromatic AlK_α radiation. The XPS spectra were calculated using MultiPak software (CasaXPS).

Catalytic testing of the catalysts was performed in a Microactivity Reactor System, PID of Eng&Tech/Micromeritics. The reactor was a quartz tube of 320 mm in length and 12.7 mm in diameter. No pre-treatment was done on the catalysts before testing. The products were then analysed by gas chromatography in an Agilent gas chromatograph 6890 equipped

with TCD (HP-PLOT/Q) and FID (Al_2O_3/KcL) detectors. The temperature ramp for the catalytic testing was 250-410°C, and products were analysed every 30°C, 20 minutes after the start of the reaction. The setup is shown in Figure 8.

Figure 8. Microactivity Reactor System PID (on the right) with Agilent Gas Chromatograph (left). Both of the instruments are outlined.

3.3. Preparation of the catalysts

For this work, mesoporous precursor iron oxide (referred to as FeO_x). was prepared via the 2-step synthesis method. The first step was the preparation of iron (II) oxalate dihydrate. In the second step, iron (II) oxalate was treated at 175°C in the air to obtain iron oxide. Next, the iron oxide substrate was impregnated with copper nanoparticles (Cu NPs), using the wet impregnation method. Cu NPs were reduced from Cu^{2+} using hydrazine. The reaction chart for each step is summarised in Equations 16, 17 and 18 below. After the preparation of the catalysts, their catalytic activity was studied during the hydrogenation of CO_2.

$$(16)$$

$$(17)$$

$$(18)$$
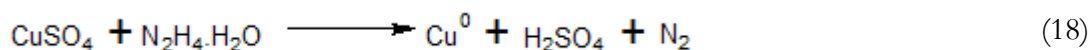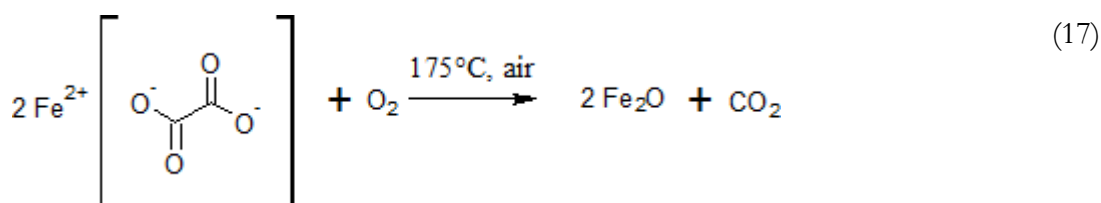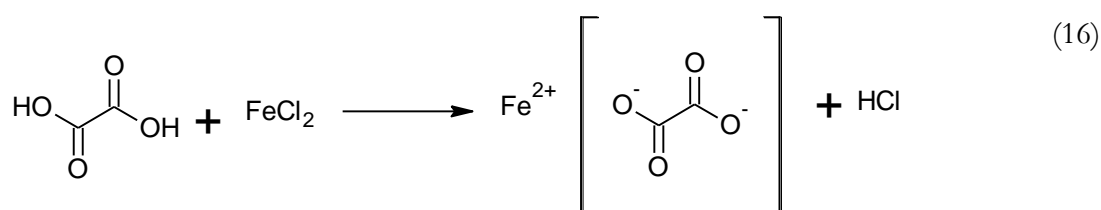
3.3.1. Preparation of FeOx substrate

The preparation of mesoporous FeO_x was a 2-step process. In the first step, iron (II) oxalate dihydrate was prepared. The second step was the treatment of the prepared yellow powder at 175°C in the air to obtain iron oxide, a reddish-brown powder. Typically, 1 mmol of oxalic acid was dissolved in 10 mL of *N,N*-dimethylacetamide. Then, a solution of 1 mmol of iron (II) chloride in 12 mL of deionized water was added at room temperature. In the case of this work, the measurements were scaled up to have a sufficient amount of iron (II) oxalate, for 1 g of resulting iron (II) oxalate, the measurements of reactants were multiplied by 8.

The reaction was completed after 5 min, and iron (II) oxalate was separated by centrifugation, for 10 minutes at 4400 rpm (rotations per minute). The precipitate was washed with deionized water and ethanol, and it was centrifuged again after each washing. The wet precipitate was then dried in a vacuum at 60°C (333 K) for 2 h. Dried yellow powder

of iron (II) oxalate was spread in a crucible in a thin layer and treated at the temperature of 175°C (448 K) in the air for 12 h to obtain FeO_x.

3.3.2. Preparation of Cu/FeO_x catalysts

The Cu/FeO_x was fabricated following the reported wet impregnation method [82]. Typically, 1 g of already prepared FeO_x was dispersed in deionized water. Then 15.7 mmol/L of an aqueous solution of copper sulphate pentahydrate was added, the volume was calculated to the desired final load of copper in catalysts. In this work, there were used 1 wt.%, 3 wt.% and 5 wt.% loads, the volume of copper sulphate solution was 2.55 ml for 1 wt.%, 7.65 ml for 3 wt.% and 12.75 ml for 5 wt.%. The total volume of liquid was 200 mL. The reactants are listed in Table 1.

After 10 min of sonication, 50 ml of 4.95 mmol/L solution of hydrazine hydrate (0.012 mL of hydrazine hydrate in 50 mL solution) was poured into the reaction mixture and was sonicated for an additional 10 min. The same amount of hydrazine was added to all reaction mixtures to rule out the influence of hydrazine on the catalytic performance. The resulting reddish-brown solid was isolated by centrifugation, washed with water and ethanol, and dried in a flow box under an inert nitrogen atmosphere at room temperature for 12 h [54, 137].

A reference catalyst (copper-free FeOx) was prepared using the same procedure however, instead of copper sulphate solution in the first step, a total volume of 200 mL of deionized water was added. After 10 min of sonication, 50 ml of 4.95 mmol/L solution of hydrazine hydrate was added. The following process was identical.

Table 1. Mass and volume of reaction chemicals used for the preparation of Cu/FeO_x catalysts and a reference catalyst.

Catalyst	FeO_x [g]	Water [mL]	$CuSO_4.5H_2O$ solution [mL]	$N_2H_4.H_2O$ solution [mL]
FeO_x	1	200	0	50
1%-Cu/FeO_x	1	147.5	2.55	50
3%-Cu/FeO_x	1	142.4	7.65	50
5%-Cu/FeO_x	1	137.3	12.75	50

The samples of the catalysts, according to their Cu content of 1%, 3% and 5%, are named as 1%-Cu/FeO$_x$,3%-Cu/FeO$_x$, 5%-Cu/FeO$_x$ respectively; the copper-free iron oxide reference sample is named FeO$_x$ throughout this thesis.

The prepared catalysts were then characterised by transmission electron microscopy (TEM), scanning electron microscopy (SEM), high-resolution transmission spectroscopy (HRTEM) with high-angle annular dark-field scanning transmission electron microscopy (STEM/HAADF), energy-dispersive X-ray spectroscopy (EDX), atomic absorption spectroscopy (AAS), X-ray diffraction (XRD), sorption of N$_2$ with Brunauer-Emmett-Teller (BET) model and X-ray photoelectron spectroscopy (XPS).

After catalysis, the catalysts were characterised again by transmission electron microscopy (TEM), scanning electron microscopy (SEM), high-resolution transmission spectroscopy (HRTEM) with high-angle annular dark-field scanning transmission electron microscopy (STEM/HAADF), energy-dispersive X-ray spectroscopy (EDX), X-ray diffraction (XRD) and sorption of N$_2$ with Brunauer-Emmett-Teller (BET) model to study chemical changes in the catalysts during hydrogenation of CO$_2$.

All results of these characterisations will be shown and described in the Results section of this work.

3.4. Catalytic testing

Study of the catalytic activity of the prepared Cu/FeO_x catalysts was performed in a Microactivity Reactor System, PID of Eng&Tech/Micromeritics having a quartz tube reactor of 320 mm in length and 12.7 mm diameter coupled. No pre-treatment was done on the catalysts before testing.

Typically, 200 mg of a catalyst was placed onto 20 mg of quartz wool in the middle of the reactor and was conditioned at 250°C in He with a flow of 30 mL/min for 40 min. The reaction mixture used contained CO_2, H_2 and He in the ratio of 1:5:4 giving 11 % and 49 % of CO_2 and H_2 in He, respectively. A total reactant gas flow of 25 mL/min was used at a pressure of 1 bar.

The products were analysed by gas chromatography using injection after 20 minutes of change to the next temperature step. In the range of 250°C to 410°C, the temperature was raised in steps of 30 C, at a rate of 5°C/min. The temperature ramp for the reaction can be seen in Figure 9. After reaching the highest temperature, the reactor was cooled to 250 °C under He. Next, the catalytic test was repeated using the identical heating ramp.
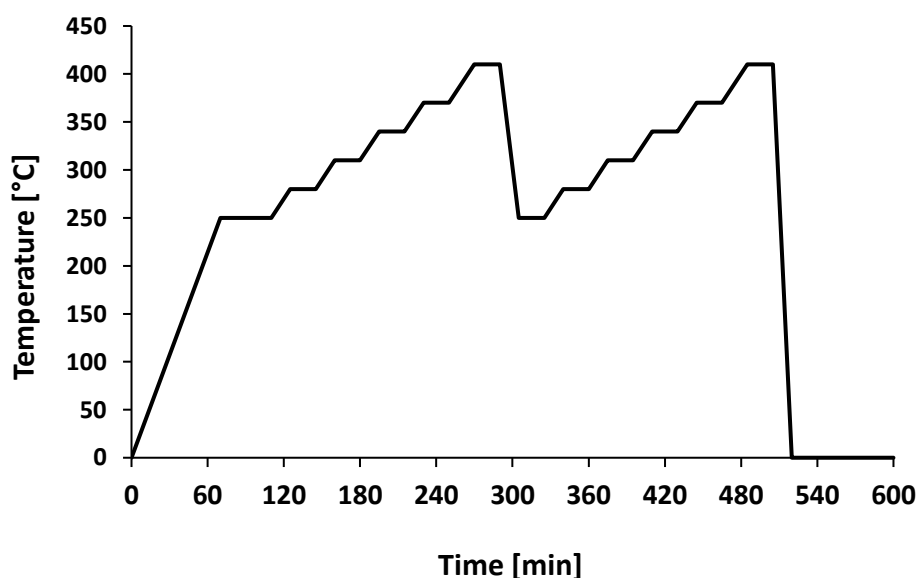

Figure 9. Temperature ramp for CO_2 hydrogenation using all Cu/FeO_x catalysts and reference.

The reaction products were analysed on an Agilent gas chromatograph 6890 equipped with TCD (HP-PLOT/Q) and FID (Al_2O_3/KcL) detectors, using an injection after 20 minutes of reaching the given temperature.

Conversion of CO_2 was calculated using the formula shown below (Equation 19). And the selectivity of individual hydrocarbon (C_i) in total hydrocarbons was calculated using Equation 20.

$$CO_2 \text{ Conversion}(\%) = \frac{CO_2 \text{ in} - CO_2 \text{ out}}{CO_2 \text{ in}} \times 100\% \tag{19}$$

$$C_i \text{ hydrocarbon selectivity (C} - \text{mol}\%) = \frac{\text{mole of } C_i \text{ hydrocarbon} \times i}{\sum_{i=1}^{n} \text{mole of } C_i \text{ hydrocarbon} \times i} \times 100 \tag{20}$$

4. Results

In this work, the study of Cu/FeO_x catalysts prepared via 2-step FeO_x synthesis and a wet impregnation of Cu NPs[82]. Prepared were 3 catalysts, 1%-Cu/FeO_x,3%-Cu/FeO_x, 5%-Cu/FeO_x and a reference FeO_x. Catalysts were characterised fresh and after being used in catalytic testing. The reaction used for this work was CO_2 hydrogenation, performed with a reaction mixture containing CO_2, H_2 and He in the ratio of 1:5:4. For each catalyst, the CO_2 conversion, hydrocarbon selectivity and selectivity to CO was calculated.

4.1. Characterization of fresh catalysts

After preparation of 1%-Cu/FeO_x,3%-Cu/FeO_x, 5%-Cu/FeO_x and FeO_x catalysts, they were left to dry in a glove box under nitrogen. Fresh catalysts, before catalytic testing, were characterized by typical characterisation techniques and the results are described in the following sections.

4.1.1. Scanning electron microscopy

SEM micrographs of FeO_x (Figure 10) show a rod-like morphology having about 5 µm in length and 1.3 µm in width. The resulting particles are coarse rods of FeO_x with a rough surface, which can attribute to multiple iron oxide morphologies.
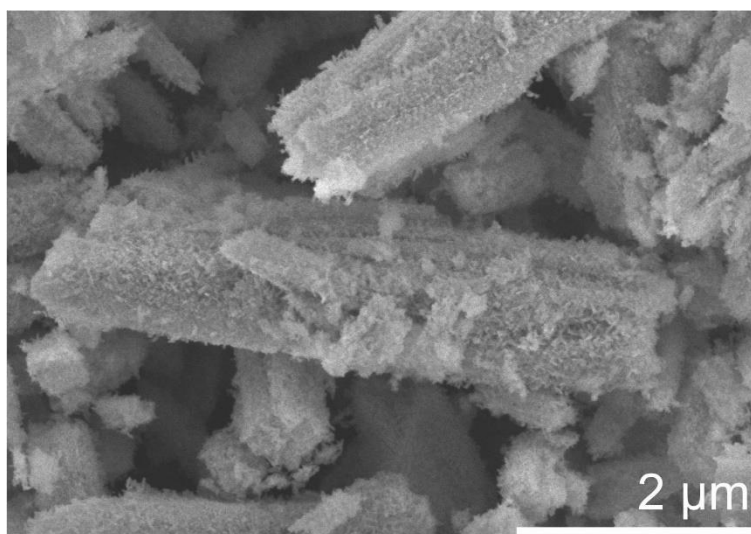

Figure 10. SEM image of fresh FeO_x.

SEM images of 1%-Cu/FeO$_x$ (Figure 11) show rod-like morphology having about 4 μm in length and 500 nm in width, here the length of the rods is comparable with copper-free FeO$_x$, but they are thinner. Upon closer observation, the surface of the rods is rough with pellet-like structures.
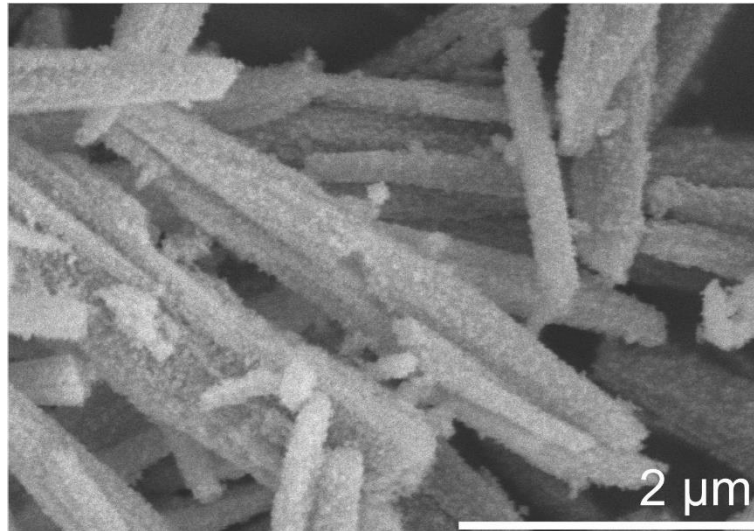
Figure 11. SEM image of 1%-Cu/FeO$_x$.

Various morphologies, some seen in this picture can be attributed to certain Fe compounds. Metallic Fe is being represented by the rod- and plate-like structures[138, 139], the flowers indicate the presence of α-Fe$_2$O$_3$, the nano-husks represent α-FeO(OH)[140] and traces of grains are typical of Fe$_3$O$_4$[141].
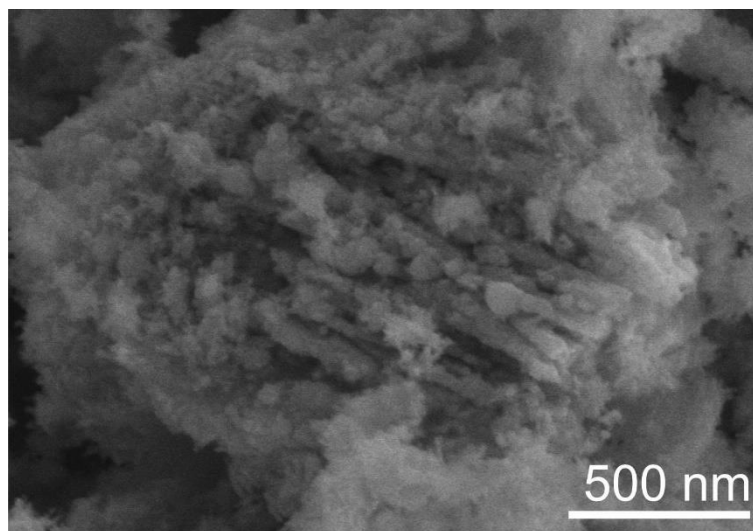
SEM images of 3%-Cu/FeO$_x$ (Figure 12) shows a continuing breakdown of the coarse structures into a congregation of needle-like structures.
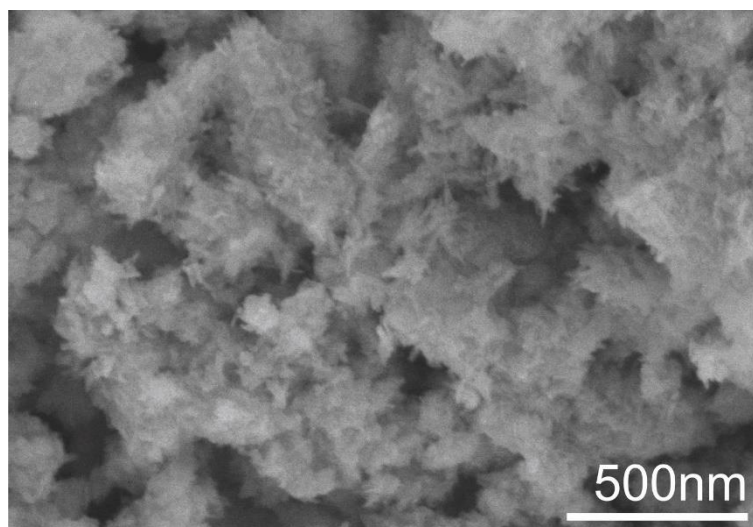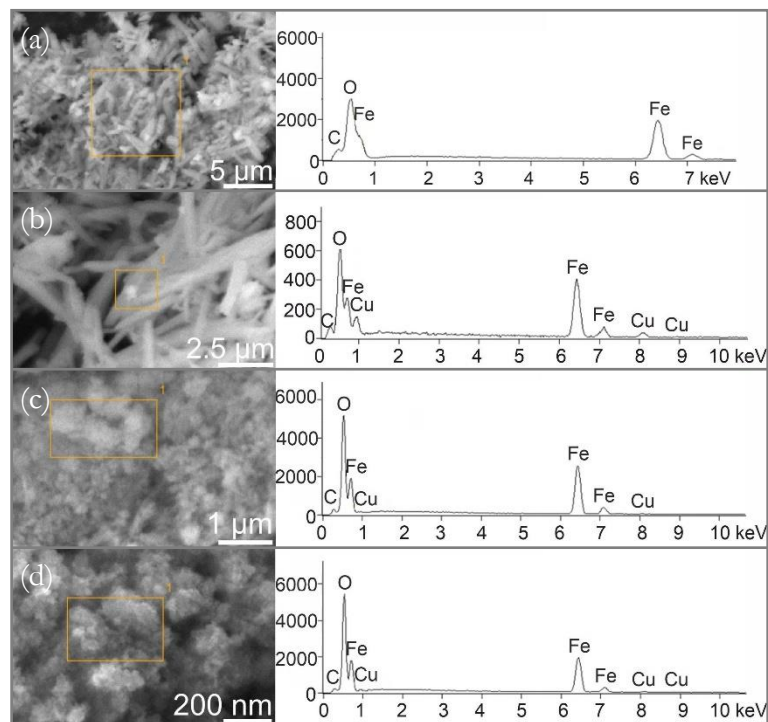

Figure 12. SEM image of 3%-Cu/FeO$_x$.

This breakdown continued for 5%-Cu/FeO$_x$ (Figure 13), but in this picture, we can recognise the same nanoneedles and on top of the base iron oxide some spherical structures.

Figure 13. SEM image of 5%-Cu/FeO$_x$.

The catalysts have different morphologies. This is partly due to the usage of hydrazine which in different concentrations can change the size of iron oxide [142]. The reduction of copper sulphate also generates sulphuric acid, which can cause the etching of iron oxide.

SEM images with EDX analysis of the selected part of the catalyst surface (Figure 14) also confirms the presence of Cu NPs on the surface of the FeO$_x$ nanorods. From the height of the peaks attributed to Cu, we can deduce the increase of copper content in different catalysts.

Figure 14. SEM images of fresh catalysts and EDX of the selected part of the image in highlighted rectangles with included particles, (a) FeO_x, (b) 1%-Cu/FeO_x, (c) 3%-Cu/FeO_x and (d) 5%-Cu/FeO_x.
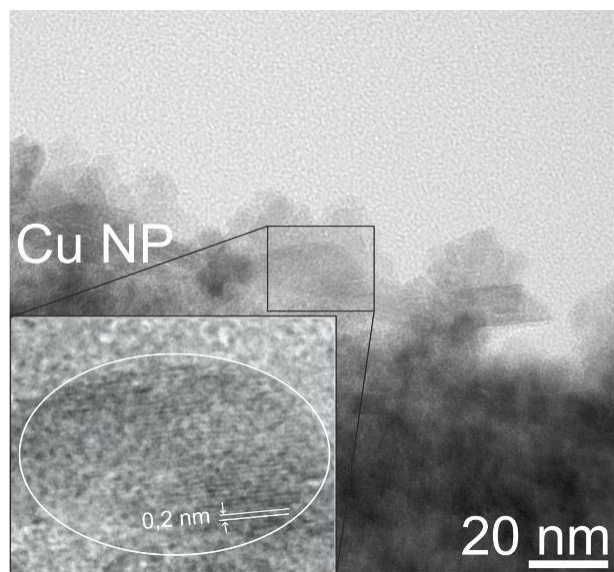
4.1.2. Transmission electron microscopy

The TEM image of FeOx is shown in Figure 15. The image shows the rod- and flower-like nanometric structures of Fe species.
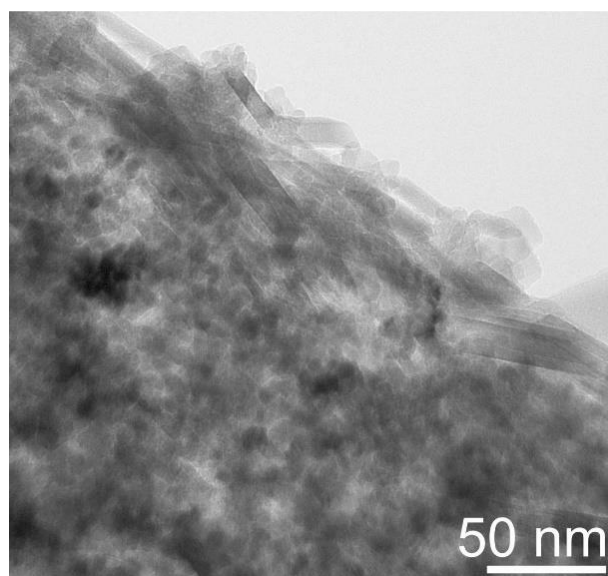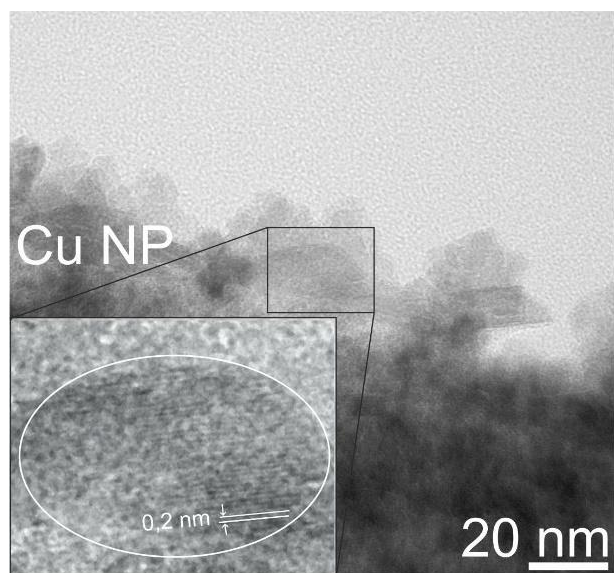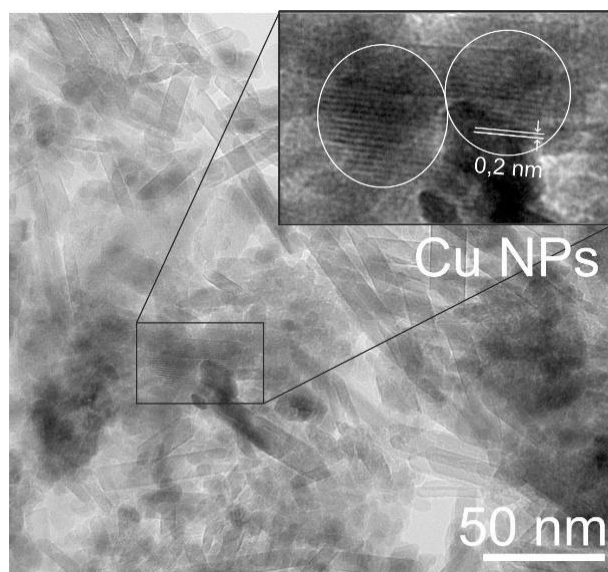

Figure 15. TEM image if fresh FeO_x

SEM image of 1%-Cu/FeO_x (Figure 16) show spherical Cu NPs with a mean diameter of 12.1 ± 4.6 nm.

Figure 16. TEM image of 1%-Cu/FeO$_x$.


Figure 17. TEM image of 3%-Cu/FeO$_x$.

Figure 18. TEM image of 5%-Cu/FeO$_x$.

Whereas, 3%-Cu/FeO$_x$ (Figure 17) and 5%-Cu/FeO$_x$ (Figure 18) have a mean diameter of 11.7 ± 2.3 nm and 13.7 ± 4.1 nm, respectively. For the Cu NP mean diameter, multiple distinct particles were counted across multiple TEM images. The images reveal the rod-like structure of FeO$_x$ and roughly spherical Cu NPs with lattice fringe spacing of 0.20 nm, corresponding to the (111) plane of copper[143].

4.1.3. High-resolution transmission spectroscopy

STEM/HAADF imagining of fresh 5%-Cu/FeO$_x$ with elemental mapping and EDX analysis, as shown in, show the presence of FeO$_x$ nanorods and other nanostructures, previously described, with sizes ranging depending on the structure from around 11 nm to around 49 nm in length (Figure 19a-f)

The chemical components of iron oxide support are apparent from images (c) and (d), where is presented an overlap of Fe and O elements. The mapping of copper is shown in the image (e), where copper is dispersed uniformly in the catalyst. The detected copper particulates are shown to be around 2 nm in diameter, which does not correlate with the size of the copper particles detected by other methods. The reason for this can be that copper exists as larger particles and smaller particles (or copper clusters) but, in this map, only the accumulated smaller particles were shown.
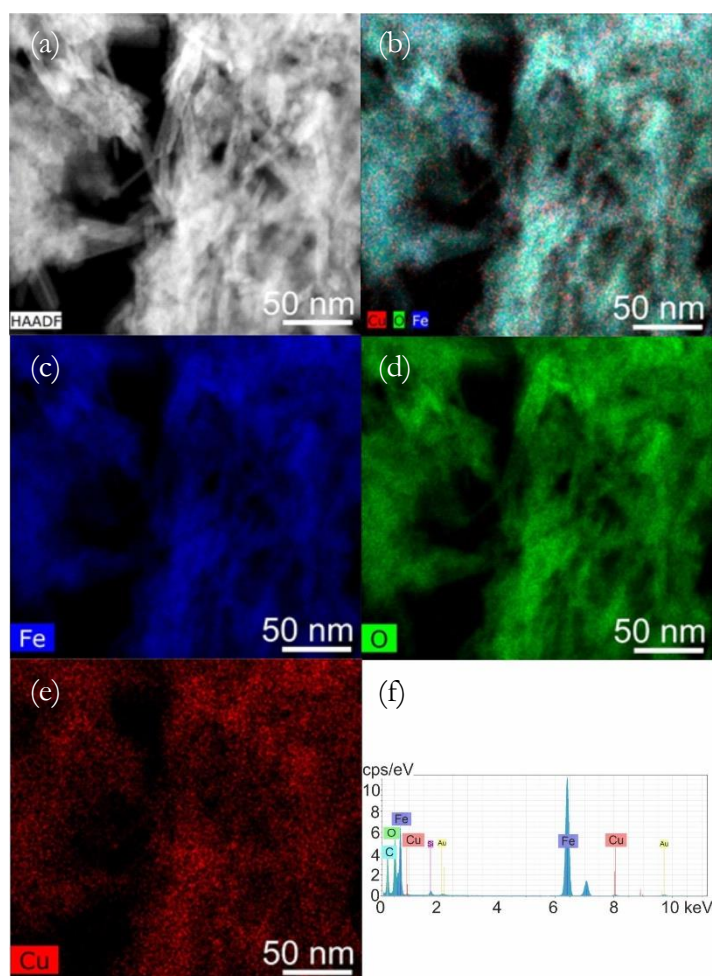
Figure 19. (a) STEM-HAADF of fresh 5%-Cu/FeO$_x$, (b-f) EDX elemental mapping of Fe, O, Cu and their overlap in fresh 5%-Cu/FeO$_x$.

4.1.4. Atomic absorption spectroscopy

AAS analysis of the catalysts was conducted to determine the precise copper content in the catalysts, the results of which are summarised in Figure 20, 1%-Cu/FeO$_x$ having 0.7% of total Cu content, while 3%-Cu/FeOx had 2.7% Cu and 5%-Cu/FeO$_x$ had 5.3% Cu.
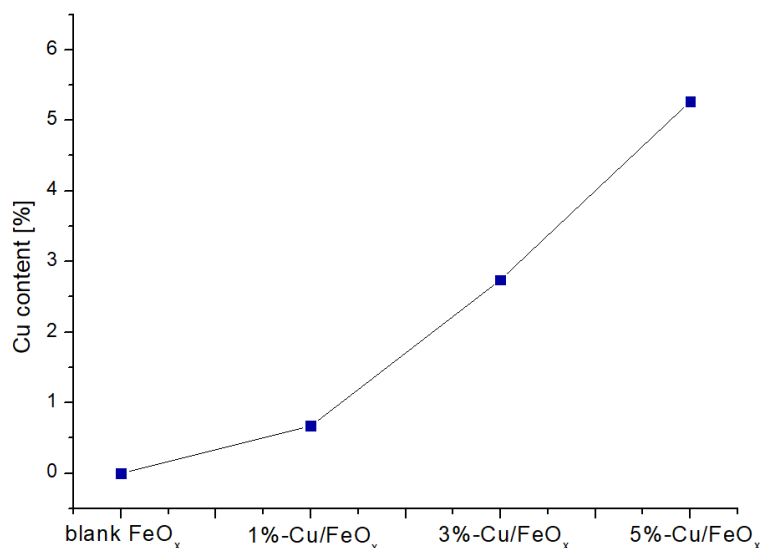
Figure 20. AAS analysis to determine copper content in fresh catalysts FeO$_x$, 1%-Cu/FeO$_x$, 3%-Cu/FeO$_x$ and 5%-Cu/FeO$_x$. The catalysts contain 0%, 0.7%, 2.7% and 5.3% of copper in their structure, respectively.

4.1.5. Powder x-ray diffraction

The quantification of the individual Fe components in the fresh and used catalysts was performed by using Rietveld analysis of the obtained XRD data, with High Score Plus (Malvern Panalytical) software utilizing the PDF-4+ and ICSD databases. XRD data are shown in Figure 21. The course of the spectra reflects the structure and morphology of the catalysts.

The fractions of different iron oxides present in the samples are summarised in Table 2. FeO$_x$ consists of 54.4% β-FeO(OH), 43.5% α-Fe$_2$O$_3$ and 2.1% Fe$_3$O$_4$. Whereas, 1%-Cu/FeO$_x$ has 81.2% α-Fe$_2$O$_3$ and 16.8% β-FeO(OH), and 3%-Cu/FeO$_x$ catalyst represented a mixture of 43.6% α-Fe$_2$O$_3$ and 56.4%, β-FeO(OH). 5%-Cu/FeO$_x$ has 51.7% β-FeO(OH) and 48.3% α-Fe$_2$O$_3$. The remaining to 100% is copper.

The presence of additional diffraction peaks at 48° and 68.4° confirmed the presence of copper[144]. XRD analysis reflects morphologies shown in SEM images of catalysts. 3%-Cu/FeO$_x$ and 5%-Cu/FeO$_x$ exhibited a similar "woolly" structure, which we can conclude

correlates with their similar composition. In contrast, blank FeO_x presents here a content of magnetite, which stem from the reduction of FeO(OH) by hydrazine. The composition of 1%-Cu/FeO_x also reflects morphology shown in SEM images, with the majority of Fe_2O_3 which formed micrometric rods.
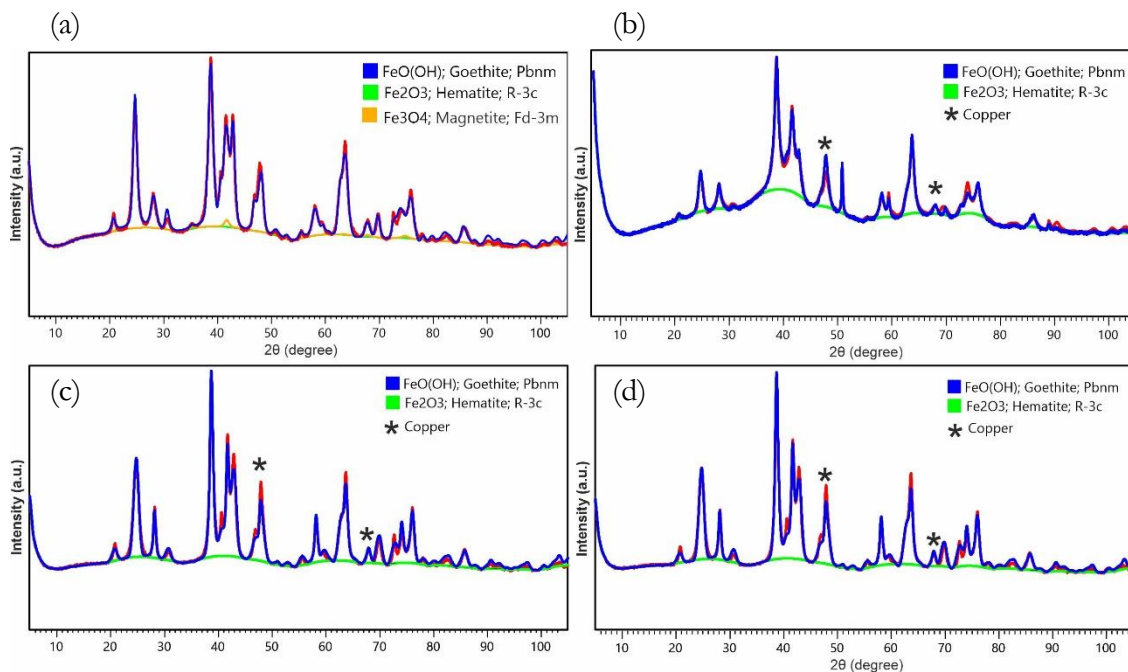
Figure 21. XRD patterns of fresh (A) FeO_x, (B) 1%-Cu/FeO_x, (C) 3%-Cu/FeO_x and (D) 5%-Cu/FeO_x.

Table 2. Fractions of various forms of iron oxide components in the fresh catalysts, obtained from XRD data using Rietveld refinement of analysis.

Catalyst	α-Fe_2O_3 [%]	β-FeO(OH) [%]	Fe_3O_4 [%]
FeO_x	43.5	54.4	2.1
1%-Cu/FeO_x	81.8	17.4	0.0
3%-Cu/FeO_x	42.2	55.1	0.0
5%-Cu/FeO_x	45.6	49.1	0.0

From XRD data, there can be obtained mean sizes of coherent domains, which for nanoparticles (that are single-domain) are smaller than their actual size, because it does not take into account the surface layer where particle loses its crystallinity. The mean x-ray coherence length (MLC) is assessed for each phase on its own, in the case of a multiphase

system, these data may not be accurate. The data can be found in Table 3. FeO_x consists of coherent domains length of 12 nm for β-FeO(OH), 9 nm for α-Fe_2O_3 and 11 nm for Fe_3O_4. Whereas, 1%-Cu/FeO_x has 12 nm for α-Fe_2O_3 and 11 nm for β-FeO(OH) and (not in the table) 56 nm for copper phase, and 3%-Cu/FeO_x catalyst 19 nm for α-Fe_2O_3 and 9 nm for β-FeO(OH). 5%-Cu/FeO_x has 19 nm β-FeO(OH) and 10 nm α-Fe_2O_3.

Table 3. Mean X-ray coherence length of fresh catalysts obtained from XRD data using Rietveld refinement of analysis.

| Catalyst	α-Fe_2O [nm]	β-FeO(OH) [nm]	Fe_3O_4 [nm]
FeO_x	9	12	11
1%-Cu/FeO_x	12	11	0.0
3%-Cu/FeO_x	19	9	0.0
5%-Cu/FeO_x	19	10	0.0

4.1.6. Specific surface area based on sorption of N_2

Adsorption-desorption isotherms (Figure 22) were tested at 77 K up to saturation pressure of nitrogen to determine the precise surface area of the prepared catalysts (Brunauer-Emmett-Teller, BET). The hysteresis of the two curves shows that the prepared catalysts are porous.

The specific surface area of the catalysts was calculated to be 114 m^2/g for blank FeOx, 114 m^2/g for 1%-Cu/FeO_x, 93 m^2/g for 3%-Cu/FeOx and 92 m^2/g for 5%-Cu/FeO_x. The data are summarised in Table 4.

The difference in morphologies of catalysts presents itself in BET as well. The "woolly" structure of 3%-Cu/FeO_x and 5%-Cu/FeO_x contains the nanoneedles and nanospheres, however, the active surface seems to be blocked by these complex morphologies. In contrast, FeO_x and 1%-Cu/FeO_x as shown in SEM images, have the surface of rods roughened, which increased their specific surface area. The etching caused by sulphuric acid generated during the reduction of copper sulphate caused that the surface of iron oxide is getting filled out, the roughness is decreasing and naturally, the increase of specific surface area.
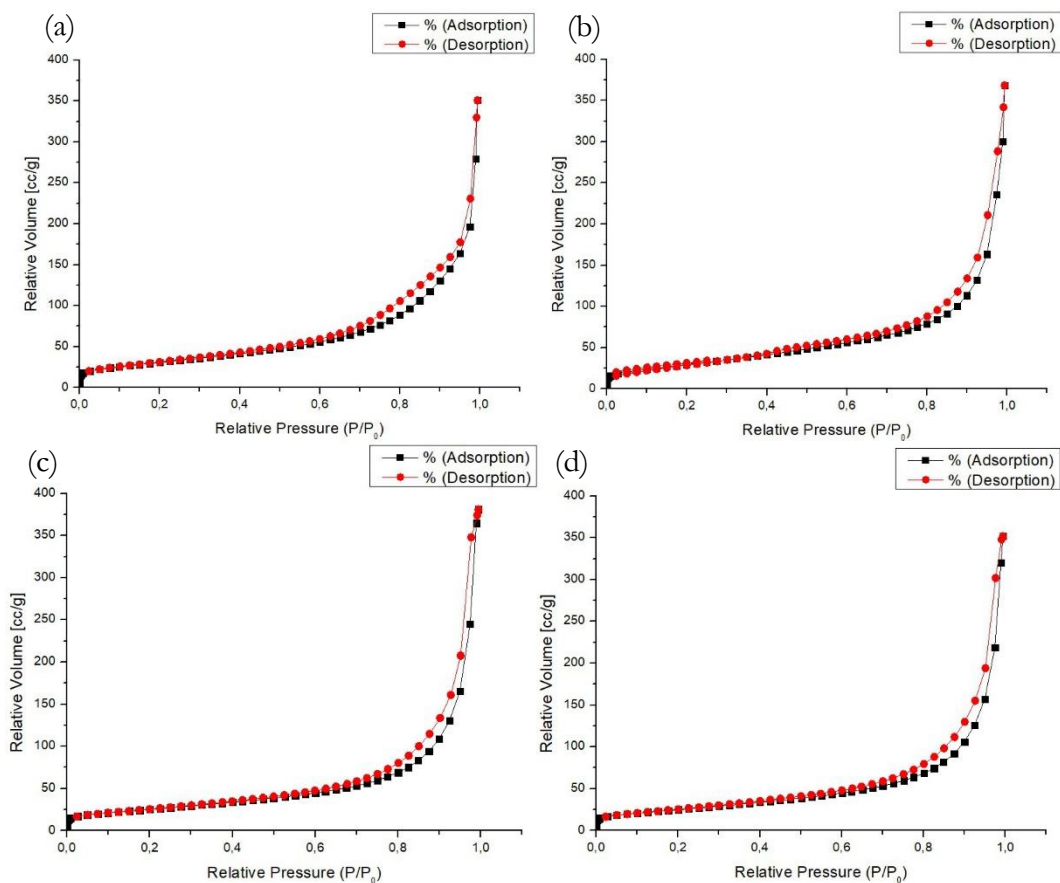
Figure 22. Adsorption and desorption isotherms of fresh (a) blank FeO_x, (b) 1%-Cu/FeO_x, (c) 3%-Cu/FeO_x and (d) 5%-Cu/FeO_x.

Table 4. Specific surface area of fresh catalysts as determined from adsorption/desorption of nitrogen on the surface of the fresh catalysts. Multipoint BET was assessed using Rouquerol method

Catalyst	Specific surface area [m²/g]
FeO_x	114
1%-Cu/FeO_x	114
3%-Cu/FeO_x	93
5%-Cu/FeO_x	92

4.1.7. X-ray photoelectron spectroscopy

The XPS analysis was performed to analyse the chemical composition of the samples' surfaces and to determine the valence state of copper. Figure 23a, c and e show the survey spectra with the quantification (at. %) of the catalysts 1%-Cu/FeO$_x$, 3%-Cu/FeO$_x$ and 5%-Cu/FeO$_x$, respectively.
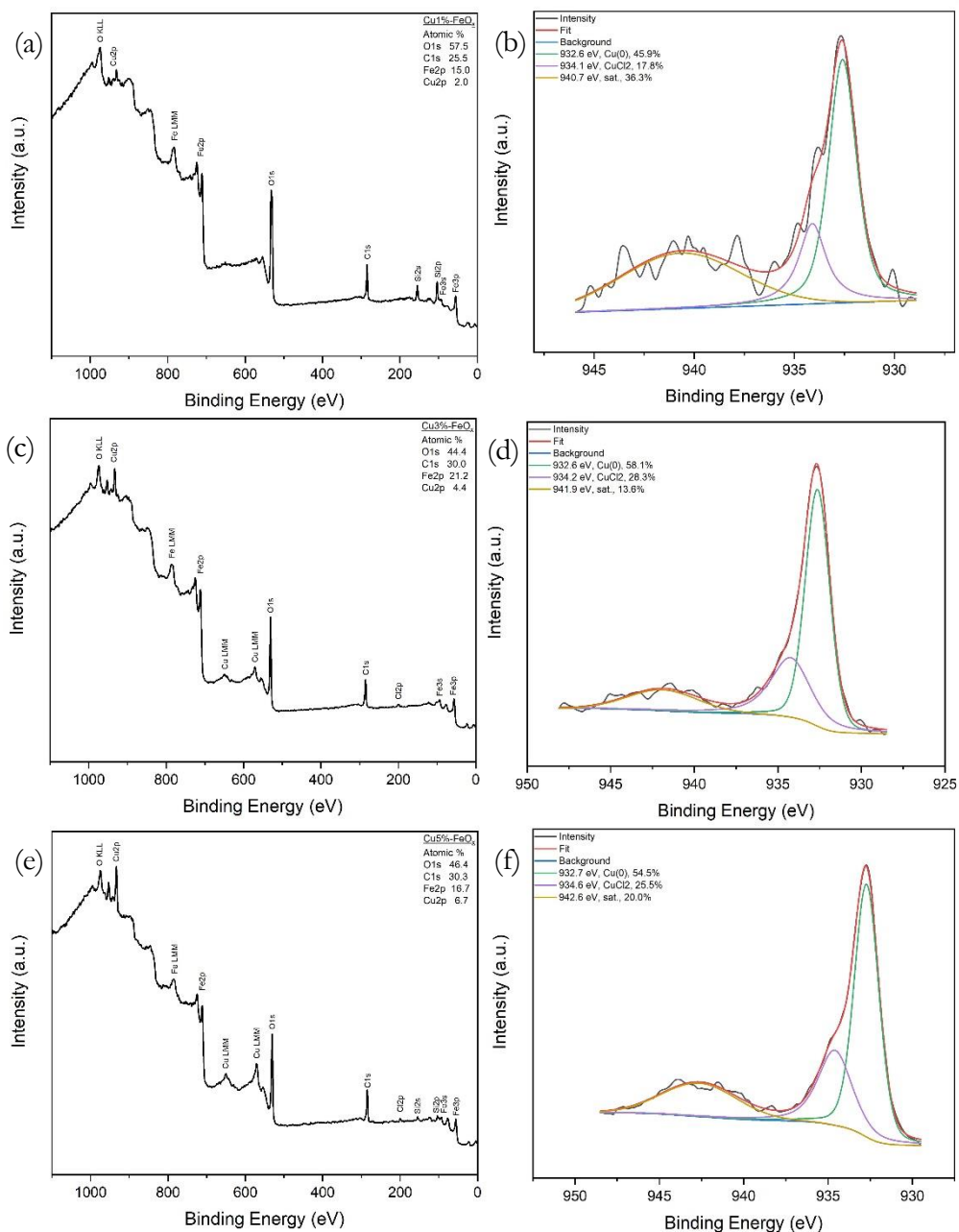
Figure 23. XPS analysis; quantification and deconvoluted spectra of copper for catalysts (a,b) 1%-Cu/FeO$_x$, (c, d) 3%-Cu/FeO$_x$ and (e, f) 5%-Cu/FeO$_x$.

The deconvoluted high-resolution spectra of copper (Cu $2p_{3/2}$) for each catalyst 1%-Cu/FeO$_x$, 3%-Cu/FeO$_x$ and 5%-Cu/FeO$_x$, are shown in figure S4B, D and F. All spectra can be deconvoluted by two main components and one satellite feature. The components at binding energy around 932.6 eV are related to Cu(0), while the components at binding energies ranging from 934.1 eV to 934.6 eV reflect the presence of CuCl$_2$. The spectral features above 940.0 eV are satellites related to Cu^{2+} in CuCl$_2$.[145, 146] The presence of chlorides can be due to the imperfect washing after synthesis of iron oxalate, one of the precursors was iron (II) chloride. Remaining chloride then reacted with reduced copper in the next preparation step.

4.2. Catalytic testing of prepared catalysts

To study catalytic activity of FeO_x and Cu/FeO_x catalysts, a series of tests were performed in a quartz tube reactor (Microactivity Reactor System-PID Eng&Tech/Micromeritics). 200 mg of catalyst was placed in the middle of the tube on a quartz wool. The gas mixture introduced to the reactor contained CO_2, H_2 and He in a 1:5:4 ratio with a total flow 25 mL/min. The temperature range of the reaction was 250 – 410°C in two consecutive temperature ramps, with product detection in 30°C intervals.

4.2.1. Reference FeO_x

Figure 24 shows the evolution of CO_2 conversion and product selectivities during the temperature ramp applied for the FeO_x catalyst. At 250 °C, 1.5 % CO_2 conversion was observed with 100% selectivity to CH_4. At 280°C, a slight increase in conversion to 2.0% was detected with 100% CH_4 selectivity (See plots in **Figure 24**b). At 310°C, the conversion rose to 3 % and the onset of the production of C_2-C_4 olefins was observed along with the dominant methane production, with a C_2-C_4 selectivity of 9.0%. With further temperature increase, additional hydrocarbon products emerged with both CO_2 conversion and overall selectivities towards the products gaining as follows. At 340°C, 7.9% CO_2 conversion and hydrocarbons selectivities of 26.2%, 18.0%, CH_4 C_2-C_4 paraffins 36.4% C_2-C_4 olefins and 19.5%. C_5^+. At 370°C, CO_2 conversion reached 14.8%, accompanied by selectivities of 19.2% CH_4, 22.7% C_2-C_4 paraffins, 31.9% C_2-C_4 olefins and 26.2% C_5^+ hydrocarbons. At 410 °C CO_2 conversion went up to 30.3% both product selectivities of 9.7% CH_4, 25% C_2-C_4 paraffins, 31.6% C_2-C_4 olefins and 13.7% C_5^+. No CO was detected.

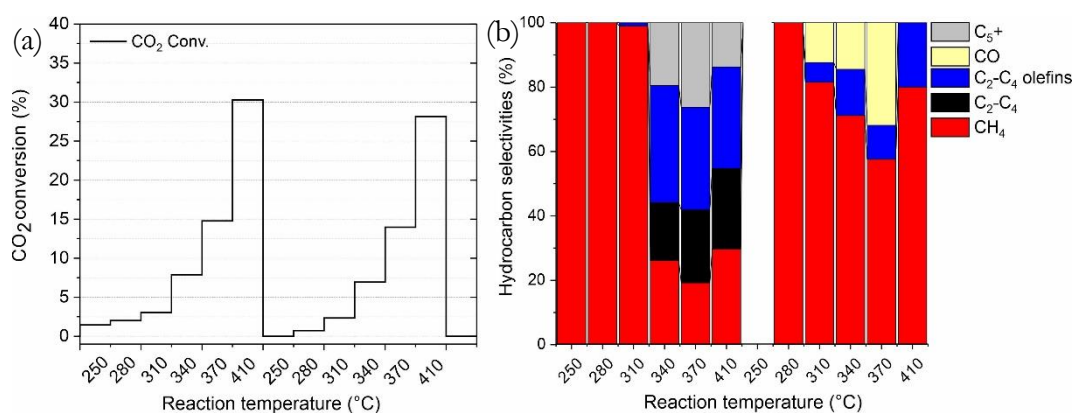**Figure 24.** Hydrogenation of CO2. CO2 conversion and hydrocarbon selectivities by FeO_x.

After the 410°C step, the reactor was cooled down to 250°C under He atmosphere, the identical temperature ramp was applied again. The main findings from the second temperature ramp are as follows. For 250, 280, 310, 340, 370 and 410°C, the CO_2 conversion was 0%, 0.7%, 2.4%, 6.9%, 14% and 28.2 % respectively, accompanied by the depletion of C_2-C_4 paraffins and C_5^+ hydrocarbons and the appearance of CO with up to 32% selectivity at 370°C.

4.2.2. Cu/FeOₓ catalysts - Temperature ramp I

In the case of the Cu/FeOx samples, as shown in Figure 25, the incorporation of Cu NPs onto FeOx lead to an increase in both conversion and selectivity towards higher hydrocarbons. At 250°C, no CO_2 conversions were observed for 1%-Cu/FeO$_x$, but at the same temperature 3%-Cu/FeO$_x$ and 5%-Cu/FeO$_x$ while 2.3% and 1.3% CO2 conversion, with CH_4 as the sole product.

At 280°C, 1%-Cu/FeO$_x$ still showed no activity, while for 3%-Cu/FeO$_x$ and 5%-Cu/FeO$_x$ CO_2 conversion went up to 6.2% and 5.6%, respectively. 3%-Cu/FeO$_x$ produced 83% CH_4 , 5.3% C_2-C_4 paraffins and 3.4% CO; and 5%-Cu/FeO$_x$ generated 76.6% CH_4, 8.6% C_2-C_4 paraffins, 7.7% C_2-C_4 olefins and 7.1% CO.

At 310°C 3.5%, 13% and 12% CO_2 conversions were achieved with 1%-Cu/FeO$_x$, 3%-Cu/FeO$_x$ and 5%-Cu/FeO$_x$ catalysts, respectively. 1%-Cu/FeO$_x$ produced 32.3% CH_4, 13.7% C_2-C_4 paraffins, 50.1% C_2-C_4 olefins and 3.9% C_5^+. 3%-Cu/FeO$_x$ produced 67% CH_4, 11.8% C_2-C_4 paraffins, 17% C_2-C_4 olefins, 1.3% C_5^+ and 2.9% CO; and 5%-Cu/FeO$_x$ generated 68.8% CH_4, 18% C_2-C_4 paraffins, 9% C_2-C_4 olefins, 1.3% C_5^+ and 2.8% CO.

At 340°C, 14.7%, 19.1% and 19.9% CO_2 conversions were achieved with 1%-Cu/FeO$_x$, 3%-Cu/FeO$_x$ and 5%-Cu/FeO$_x$ catalysts, respectively. 1%-Cu/FeO$_x$ produced 52.6% CH_4, 13.2% C_2-C_4 paraffins, 26% C_2-C_4 olefins, 5.3% C_5^+ and 2.9% CO. 3%-Cu/FeO$_x$ produced 64.4% CH_4, 14.8% C_2-C_4 paraffins, 16.1% C_2-C_4 olefins, 1.8% C_5^+ and 2.8% CO; and 5%-Cu/FeO$_x$ generated 67.8% CH_4, 20.4% C_2-C_4 paraffins, 6.2% C_2-C_4 olefins, 1.5% C_5^+ and 4.2% CO.

At 370°C, 23.5%, 27.3% and 27.7% CO_2 conversions were achieved with 1%-Cu/FeO$_x$, 3%-Cu/FeO$_x$ and 5%-Cu/FeO$_x$ catalysts, respectively. 1%-Cu/FeO$_x$ produced 66.9% CH_4, 3.1% C_2-C_4 paraffins, 28.5% C_2-C_4 olefins, and 2.9% CO. 3%-Cu/FeO$_x$ produced 64% CH_4,

17.6% C_2-C_4 paraffins, 14.1% C_2-C_4 olefins, 1.6% C_5^+ and 2.8% CO; and 5%-Cu/FeO$_x$ generated 79.1% CH_4, 12.2% C_2-C_4 paraffins, 4.1% C_2-C_4 olefins, 0.1% C_5^+ and 4.5% CO.

At 410°C, 34.8%, 36.5% and 34.9% CO_2 conversions were achieved with 1%-Cu/FeO$_x$, 3%-Cu/FeO$_x$ and 5%-Cu/FeO$_x$ catalysts, respectively. 1%-Cu/FeO$_x$ produced 76.6% CH_4, 1.7% C_2-C_4 paraffins, 19% C_2-C_4 olefins, and 3.2% CO. 3%-Cu/FeO$_x$ produced 83.4% CH_4, 6.2% C_2-C_4 paraffins, 6.5% C_2-C_4 olefins, 0.2% C_5^+ and 3.7% CO; and 5%-Cu/FeO$_x$ generated 92.9% CH_4, 2.2% C_2-C_4 paraffins and 5.1% CO.

4.2.3.   Cu/FeO$_x$ catalysts - Temperature ramp II

At 250°C, 1.4%, 7.3% and 5.6% CO_2 conversions were achieved with 1%-Cu/FeO$_x$, 3%-Cu/FeO$_x$ and 5%-Cu/FeO$_x$ catalysts, respectively. 1%-Cu/FeO$_x$ produced 68.7% CH_4, 23.4% C_2-C_4 paraffins, 6.2% C_2-C_4 olefins and 1.7% CO. 3%-Cu/FeO$_x$ produced 63.8% CH_4, 32.4% C_2-C_4 paraffins, 2.8% C_5^+ and 2.8% CO; and 5%-Cu/FeO$_x$ generated 58.6% CH_4, 37.3% C_2-C_4 paraffins, 0.3% C_2-C_4 olefins, 2.9% C_5^+ and 2.6% CO.

At 280°C, 3.4%, 10.9% and 11.8% CO_2 conversions were achieved with 1%-Cu/FeO$_x$, 3%-Cu/FeO$_x$ and 5%-Cu/FeO$_x$ catalysts, respectively. 1%-Cu/FeO$_x$ produced 68.1% CH_4, 18.5% C_2-C_4 paraffins, 10.5% C_2-C_4 olefins, 1.3% C_5^+ and 1.7% CO. 3%-Cu/FeO$_x$ produced 58.3% CH_4, 34.4% C_2-C_4 paraffins, 2.2% C_2-C_4 olefins, 2.4% C_5^+ and 2.6% CO; and 5%-Cu/FeO$_x$ generated 55.3% CH_4, 36.5% C_2-C_4 paraffins, 1.8% C_2-C_4 olefins, 3.9% C_5^+ and 2.5% CO.

At 310°C, 8.3%, 17.2% and 17% CO_2 conversions were achieved with 1%-Cu/FeO$_x$, 3%-Cu/FeO$_x$ and 5%-Cu/FeO$_x$ catalysts, respectively. 1%-Cu/FeO$_x$ produced 64.5% CH_4, 14.8% C_2-C_4 paraffins, 17.4% C_2-C_4 olefins, 2.5% C_5^+ and 0.7% CO. 3%-Cu/FeO$_x$ produced 56.3% CH_4, 32.2% C_2-C_4 paraffins, 5.6% C_2-C_4 olefins, 3.6% C_5^+ and 2.3% CO; and 5%-Cu/FeO$_x$ generated 54.1% CH_4, 35.1% C_2-C_4 paraffins, 3.5% C_2-C_4 olefins, 4.1% C_5^+ and 3.2% CO.

At 340°C, 13%, 22.9% and 23.7% CO_2 conversions were achieved with 1%-Cu/FeO$_x$, 3%-Cu/FeO$_x$ and 5%-Cu/FeO$_x$ catalysts, respectively. 1%-Cu/FeO$_x$ produced 64.6% CH_4, 9.7% C_2-C_4 paraffins, 22.8% C_2-C_4 olefins, 2.2% C_5^+ and 0.7% CO. 3%-Cu/FeO$_x$ produced 59.3% CH_4, 24.8% C_2-C_4 paraffins, 10.8% C_2-C_4 olefins, 2.9% C_5^+ and 2.3% CO; and 5%-Cu/FeO$_x$ generated 57.4% CH_4, 30% C_2-C_4 paraffins, 6.3% C_2-C_4 olefins, 3.1% C_5^+ and 3.1% CO.

At 370°C, 21.3%, 26.8% and 29.5% CO_2 conversions were achieved with 1%-Cu/FeO$_x$, 3%-Cu/FeO$_x$ and 5%-Cu/FeO$_x$ catalysts, respectively. 1%-Cu/FeO$_x$ produced 65% CH_4, 6.1% C_2-C_4 paraffins, 26.5% C_2-C_4 olefins, 1.6% C_5^+ and 0.8% CO. 3%-Cu/FeO$_x$ produced 66.5% CH_4, 14.5% C_2-C_4 paraffins, 15.2% C_2-C_4 olefins, 1.4% C_5^+ and 2.5% CO; and 5%-Cu/FeO$_x$ generated 68.7% CH_4, 18.8% C_2-C_4 paraffins, 7.2% C_2-C_4 olefins, 1.3% C_5^+ and 4.1% CO.

At 410°C, 34.3%, 36.8% and 35.6% CO_2 conversions were achieved with 1%-Cu/FeO$_x$, 3%-Cu/FeO$_x$ and 5%-Cu/FeO$_x$ catalysts, respectively. 1%-Cu/FeO$_x$ produced 75.2% CH_4, 4.3% C_2-C_4 paraffins, 17.4% C_2-C_4 olefins, 0.4% C_5^+ and 2.7% CO. 3%-Cu/FeO$_x$ produced 82.2% CH_4, 6.2% C_2-C_4 paraffins, 7.9% C_2-C_4 olefins and 3.6% CO; and 5%-Cu/FeO$_x$ generated 86.6% CH_4, 4% C_2-C_4 paraffins, 2.7% C_2-C_4 and 5.5% CO.
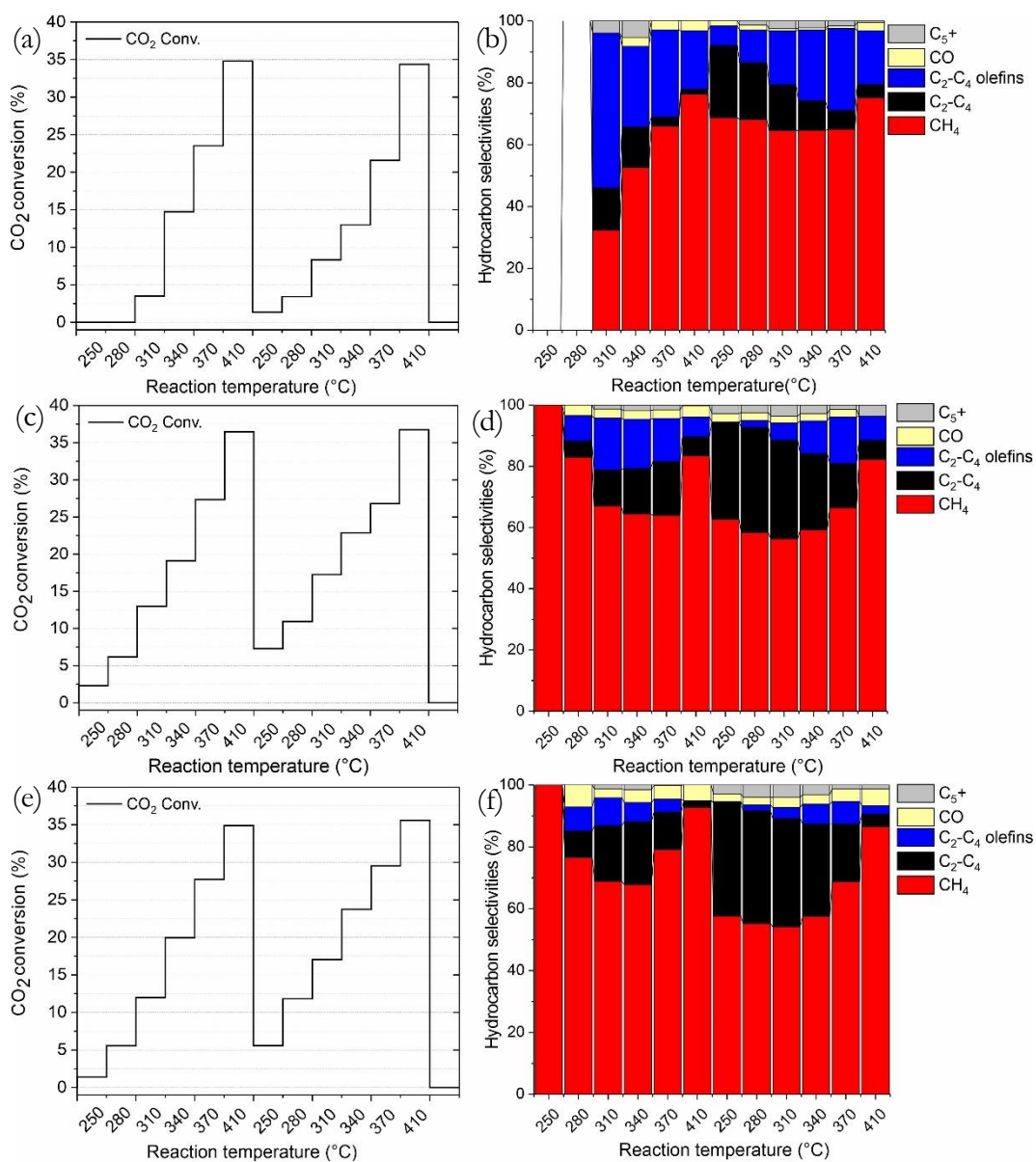
Figure 25. Hydrogenation of CO_2. CO_2 conversion and hydrocarbon selectivities by (a, b) 1%-Cu/FeO$_x$, (s, d) 3%-Cu/FeO$_x$, (e, f) 5%-Cu/FeO$_x$ catalysts. 200 mg of catalyst and $CO_2/H_2/He$ (1:5:4, total flow 25 ml/min).

4.3. Characterization of spent catalysts

Spent catalysts, after being used in CO_2 hydrogenation were characterized by scanning electron microscopy (SEM), transmission electron microscopy (TEM), high-resolution transmission spectroscopy (HRTEM) with high-angle annular dark-field scanning transmission electron microscopy (STEM/HAADF), energy-dispersive X-ray spectroscopy (EDX), X-ray diffraction (XRD) and sorption of N_2 with Brunauer-Emmett-Teller (BET) model. The results are described in the following sections.

4.3.1. Scanning electron microscopy

SEM micrographs of spent catalysts (Figure 26 for FeO_x, Figure 27 for 1%-Cu/FeO_x, Figure 28 for 3%-Cu/FeO_x, Figure 29 for 5%-Cu/FeO_x) show the transformation of the surface of the FeO_x rods, which as fresh were nonporous, into a porous one, with the large rod or wool-like structure described for fresh catalyst preserved. The surface developed intertwined polymorphs which indicate the presence of Fe_5C_2 or Fe_3C [140]. With increasing copper content, there is an apparent formation of larger counts of smaller 50 nm particles in contrast to 150 nm particles.
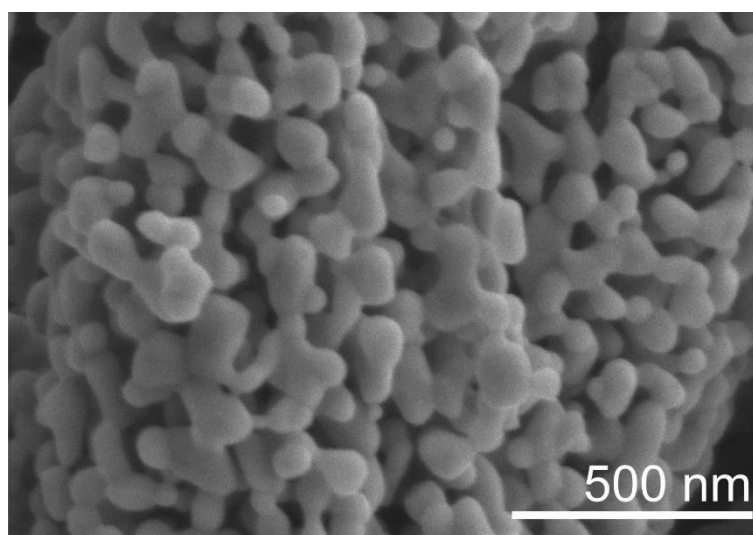
Figure 26. SEM image of spent FeO_x.

Figure 27. SEM image of spent 1%-Cu/FeO$_x$.

Figure 28. SEM image of spent 3%-Cu/FeO$_x$.

Figure 29. SEM image of spent 5%-Cu/FeO$_x$.

EDX analysis of the spent catalysts 1%-Cu/FeO$_x$, 3%-Cu/FeO$_x$ and 5%-Cu/FeO$_x$ show the increase of copper in the catalysts, from the height of the peaks attributed to copper (Figure 30).
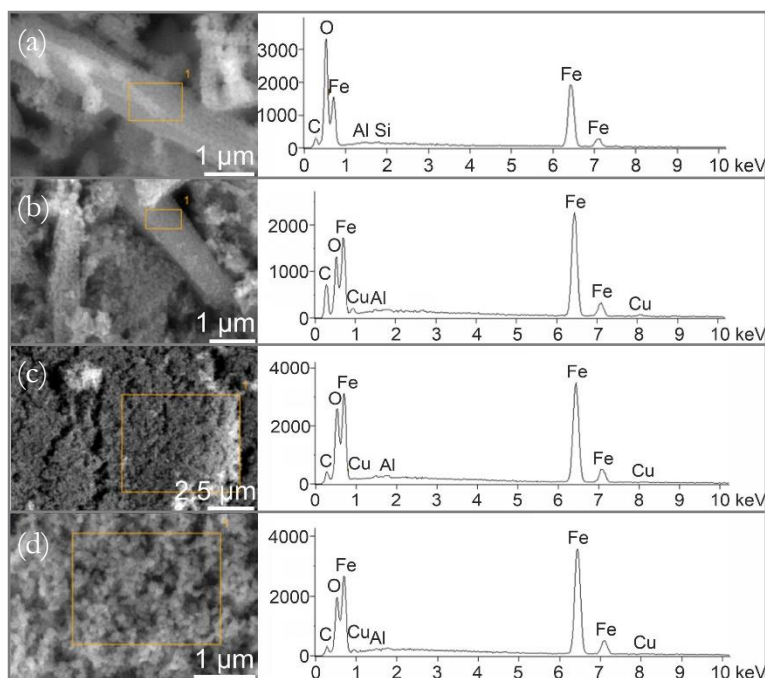
Figure 30. SEM images of the spent catalysts and EDX of the selected part of the image in highlighted rectangles with included particles, (a) spent FeO$_x$, (b) spent 1%-Cu/FeO$_x$, (c) spent 3%-Cu/FeO$_x$, (d) spent 5%-Cu/FeO$_x$.

4.3.2. Transmission electron microscopy

Figure 31 shows the TEM images of FeOx, Figure 32 shows 1%-Cu/FeO$_x$, Figure 33 shows 3%-Cu/FeOx and Figure 34 shows 5%-Cu/FeO$_x$, the images reveal a transformation of FeO$_x$ rods with (or without) Cu NPs on the surface into spherical particles. The TEM images of spent FeO$_x$ showed spherical particles with a mean diameter of 68 ± 26.8 nm.

Whereas, spent 1%-Cu/FeO$_x$, spent 3%-Cu/FeO$_x$ and spent 5%-Cu/FeO$_x$ have a mean diameter of 60.8 ± 19.2 nm, 75 ± 25.1 nm and 80.6 ± 35.5 nm, respectively. There is an apparent formation of multiple size distribution, which seem to be affected by copper content. Spent 5%-Cu/FeO$_x$ has a mean diameter of 80.6 ± 35.5 nm, with the largest particles up to 144.3 ± 6.7 nm. The surface of 5%-Cu/FeO$_x$ roughened by particulates 5 nm in diameter and with a 3nm layer of presumably carbide or carbon. It is clear that the step, which affected morphologies of fresh catalysts, was overruled by the influence of reaction (reactants and temperature) and spent catalysts. Additionally, with increasing copper content, we observe deepened difference in size distributions of smaller and larger fraction particles and a higher count of smaller particles.
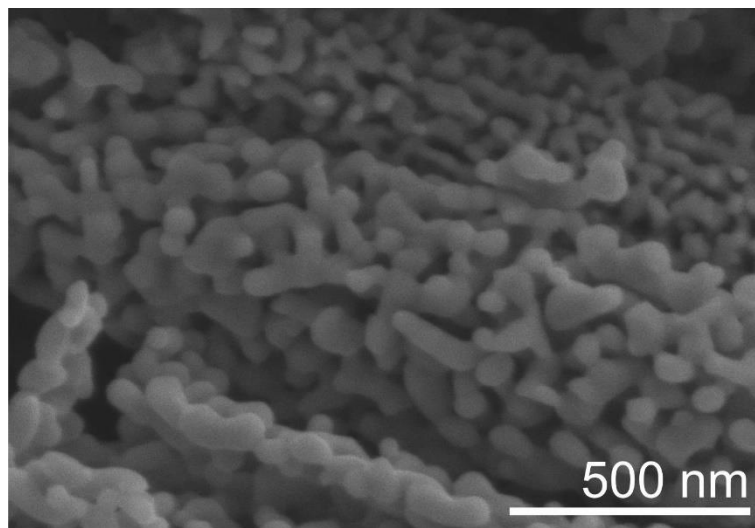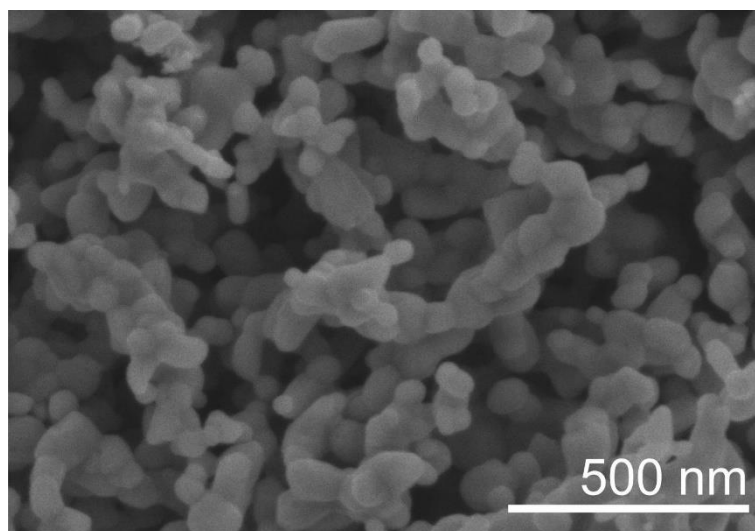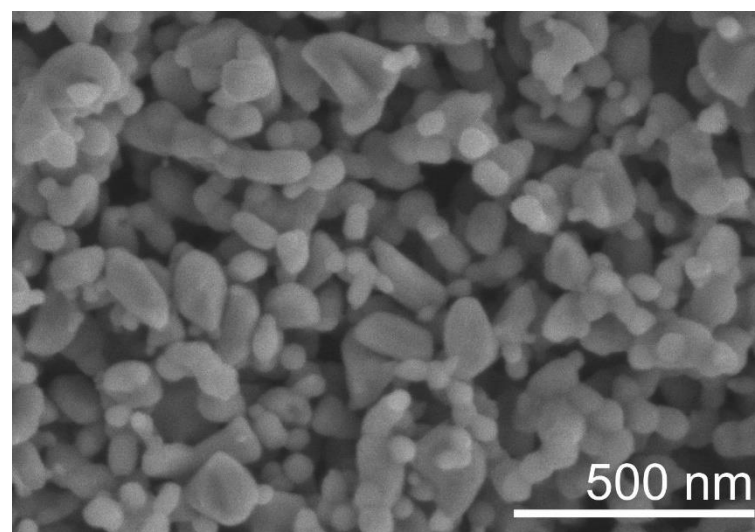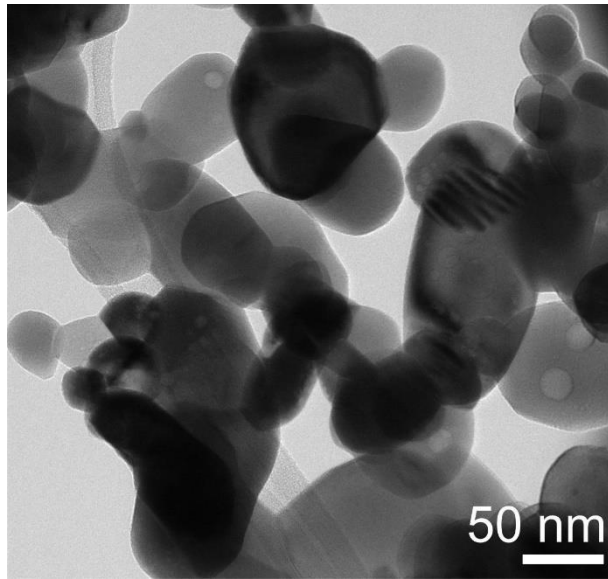
Figure 31. TEM image of spent FeO$_x$.
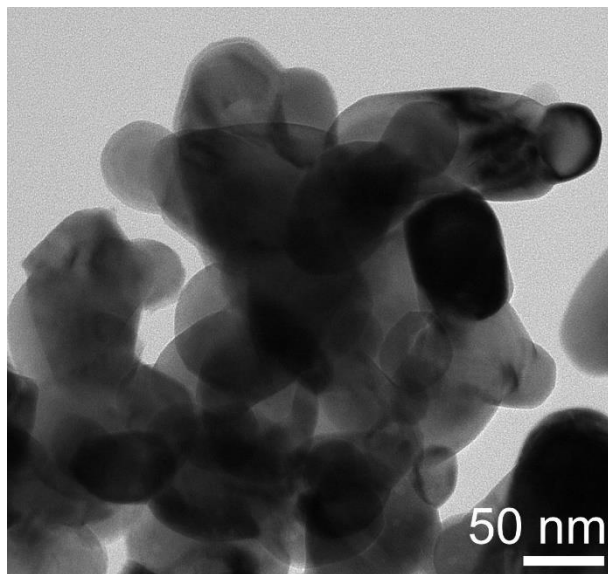
Figure 32. TEM image of spent 1%-Cu/FeO$_x$.
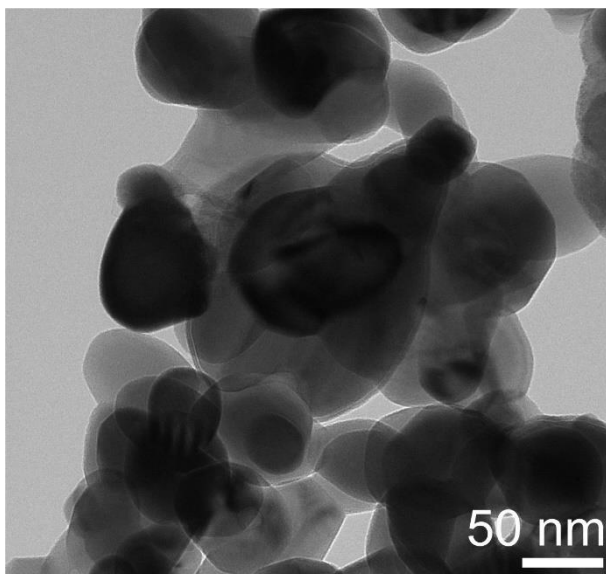
Figure 33. TEM image of spent 3%-Cu/FeO$_x$.
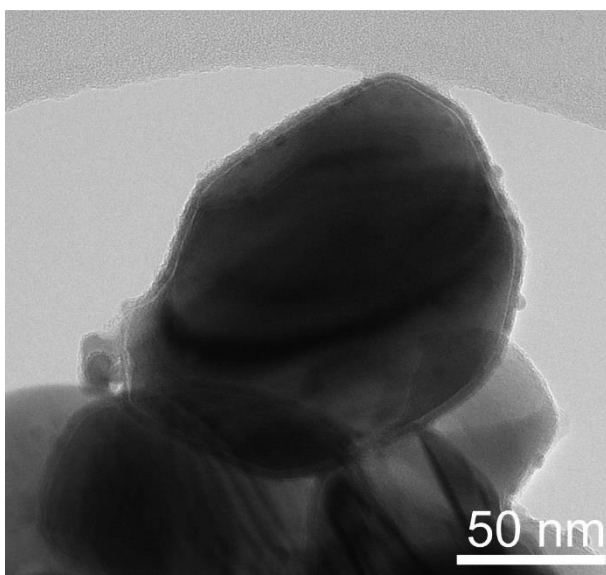
Figure 34. TEM image of spent 5%-Cu/FeO$_x$.

4.3.3. High-resolution transmission spectroscopy

STEM/HAADF imagining of spent 5%-Cu/FeO$_x$ show the presence of nanoscale Fe species of about 146 nm in diameter, with Cu nanoparticles or Cu clusters (8.4 ± 2.3 nm in diameter) on the surface, as seen in Figure 35. These images also point to the presence of atomic copper and copper oxides dispersed in the spent catalyst. In Figure 35c there is a recognisable layer of carbon (13 nm) on the surface of the particles. This indicates the deposition of carbon during catalysis, either as carbide, carbon oxide or atomic carbon.
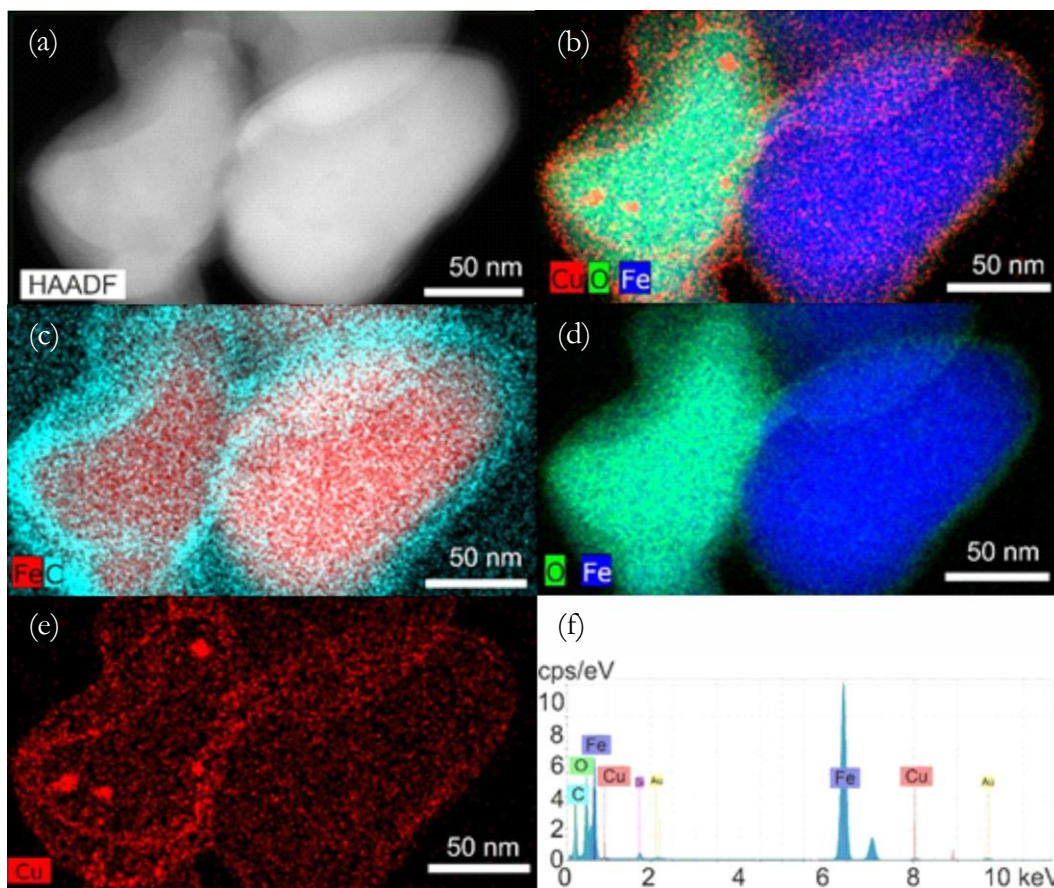
Figure 35. (a) STEM-HAADF of spent 5%-Cu/FeO$_x$, (b-f) EDX elemental mapping of Fe, O, C, Cu and their overlap in spent 5%-Cu/FeO$_x$.

4.3.4. Powder x-ray diffraction

The fractions of different iron oxides present in the samples are summarised in Table 5. Spent FeO$_x$ consists of 100% Fe$_3$O$_4$. Whereas, spent 1%-Cu/FeO$_x$ has 95% Fe$_3$O$_4$ and 4,3% Fe$_5$C$_3$ and spent 3%-Cu/FeO$_x$ catalyst represented a mixture of 71.3% Fe$_3$O$_4$ and 26% Fe$_5$C$_3$. Spent 5%-Cu/FeO$_x$ has 59.8% Fe$_3$O$_4$, 31.9% Fe$_5$C$_3$ and 3% Fe$_3$C. The remaining to 100% is copper. With the increasing copper content, there can be seen an increase of iron carbides content. The presence of additional diffraction peaks at 48° and 68.4° confirmed the presence of copper[144]. XRD data of the spent catalysts can be found in Figure 36. The presence of copper in catalysts seems to be supporting the generation of iron carbides in catalysts.
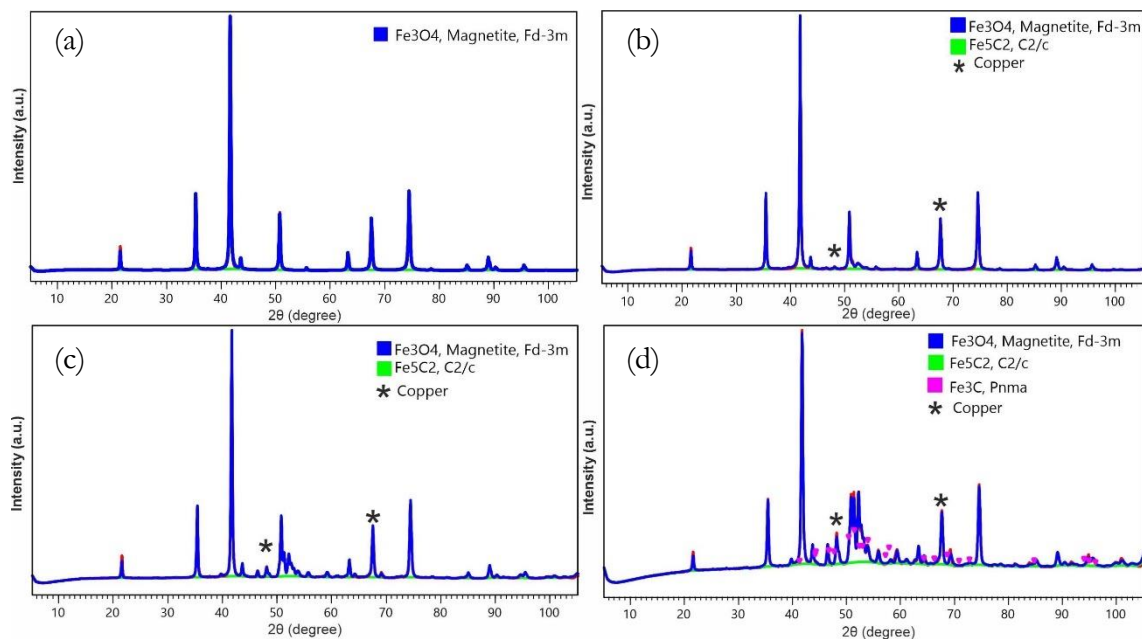
Figure 36. XRD patterns of spent (a) FeO_x, (b) 1%-Cu/FeO_x, (c) 3%-Cu/FeO_x and (d) 5%-Cu/FeO_x.

Table 5. Fractions of various forms of iron oxide components in the spent catalysts, obtained from XRD data using Rietveld refinement of analysis.

Catalyst	Fe_3O_4 [%]	Fe_5C_2 [%]	Fe_3C [%]
FeO_x	100	0.0	0.0
1%-Cu/FeO_x	95.0	4.3	0.0
3%-Cu/FeO_x	71.3	26.0	0.0
5%-Cu/FeO_x	59.8	31.9	3.0

From XRD data, we obtained the mean x-ray coherence length (MLC), which is summarised in Table 6. MLC is assessed for each phase on its own, in the case of a multiphase system, these data may not be accurate. FeO_x consists of coherent domains length of 63 nm for the Fe_3O_4 phase. Whereas, 1%-Cu/FeO_x has 63 nm for Fe_3O_4 and 29 nm for Fe_5C_2, and 3%-Cu/FeO_x has 47 nm for Fe_3O_4 and 40 nm for Fe_5C_2. 5%-Cu/FeO_x has 36 nm for Fe_3O_4, 35 nm for Fe_5C_2 and 23 nm for Fe_3C.

Table 6. Mean X-ray coherence length of spent catalysts obtained from XRD data using Rietveld refinement of analysis.

Catalyst	Fe_3O_4 [nm]	Fe_5C_2 [nm]	Fe_3C [nm]
FeO_x	63.0	0.0	0.0
1%-Cu/FeO_x	63.0	29.0	0.0
3%-Cu/FeO_x	47.0	40.0	0.0
5%-Cu/FeO_x	36.0	35.0	23.0

4.3.5. Specific surface area based on sorption of N_2

Adsorption-desorption isotherms of spent catalysts (Figure 37) were obtained at 77 K up to saturation pressure of nitrogen to determine the precise surface area of the prepared catalysts (Brunauer-Emmett-Teller, BET). As opposed to the fresh catalyst, the adsorption/desorption curves have a course that suggests that the pores present in the catalysts disappeared, due to high temperatures and ongoing reaction. The specific surface area of the catalysts was calculated to be 18.6 m^2/g for FeO_2, 18.6 m^2/g for 1%-Cu/FeO_x, 18.0 m^2/g for 3%-Cu/FeO_x and 17.4 m^2/g for 5%-Cu/FeO_x. The specific surface areas of spent catalysts are about 10 times smaller than the fresh catalysts. The data are summarised in Table 7.
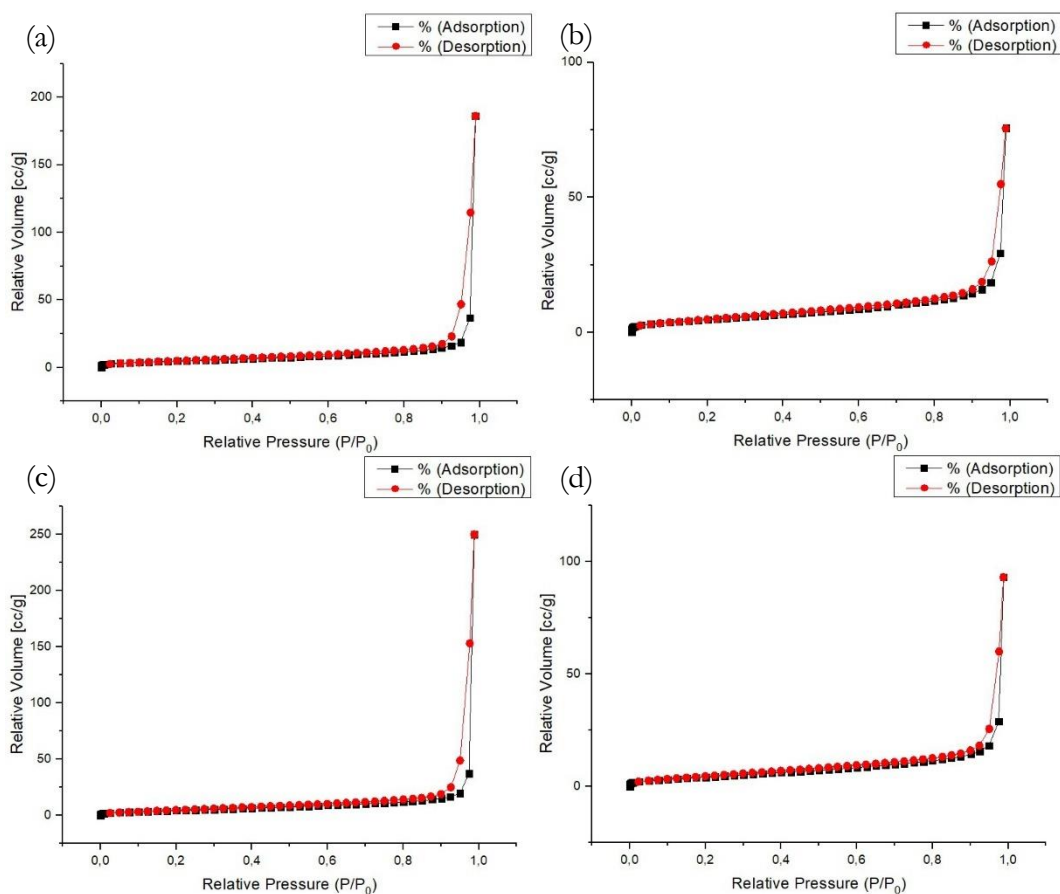
Figure 37. Adsorption and desorption isotherms of spent (a) FeO_x, (b) 1%-Cu/FeO_x, (c) 3%-Cu/FeO_x and (d) 5%-Cu/FeO_x.

Table 7. The specific surface area of spent catalysts as determined from the adsorption/desorption of nitrogen on the surface of the spent catalysts. Multipoint BET was assessed using the Rouquerol method.

Catalyst	Specific surface area [m²/g]
FeO_x	18.6
1%-Cu/FeO_x	18.6
3%-Cu/FeO_x	18.0
5%-Cu/FeO_x	17.4

5. Discussion

The subject of this diploma thesis was the catalytic hydrogenation of CO_2 on catalysts based on iron oxides. The substrate precursor FeO_x was prepared using a 2-step synthesis. In the first step, iron (II) oxalate dihydrate was prepared via precipitation. In the second preparation step, the oxalate samples were thermally decomposed in the air at a temperature of only 175 ° C. The substrate was decorated with Cu NPs following a wet impregnation procedure [82]. Three catalysts with an increasing final load of copper were prepared (and a blank).

The catalysts exhibited a rod-like morphology of iron oxide, and with increasing copper content, there was an observable breakdown of the substrate, most likely due to side products of the preparation reaction (hydrochloric acid, sulphuric acid) or directly hydrazine hydrate[142]. From blank FeO_x to 5%-Cu/FeO_x, we see a difference of the surface from coarse and clearly defined particles to almost wool. This is the effect of the abundance of hydrazine during the synthesis, which has reducing and basic properties [142]. The effect of hydrazine on catalysts is also apparent in the surface, caused by etching [147]. In the case of blank FeO_x, it was treated with hydrazine solution the same way as the other catalysts, in which hydrazine acted as a primary reducing agent of Cu^{2+}; and hydrazine hydrate caused the growth of the particles. Different composition of catalysts obtained from XRD data supports this theory, primarily with the small content of magnetite in fresh blank FeO_x exclusively. We have demonstrated the possibility of fine-tuning morphologies of FeO_x substrate for catalysis.

During CO_2 hydrogenation, with the use of blank FeO_x, we observed a decrease in CO_2 conversion in the second ramp. This may be related to the deposition of carbon on the surface of the catalyst and therefore blocking active sites of the catalyst and limiting their contact between reactant gases[148]. With the incorporation of Cu NPs in FeOx, Cu/FeOx catalysts inherit the advantages of both Cu and FeO_x in which Cu acts as a reducing metal agent and FeO_x act as an active Fischer-Tropsch catalyst.[149] It was observed that in the second ramp, the CO_2 conversion was almost double from 250-310 °C with the rise in selectivity toward C_2-C_4 hydrocarbons as compared to the first ramp where the maximum selectivity was toward CH_4 (Figure 25).

For 1%-Cu/FeO_x, the second ramp offered a relatively steady fraction of CH_4, and with rising temperature, the selectivity towards C_2-C_4 olefins was increasing at the expense of selectivity towards C_2-C_4 paraffins, as opposed to the first ramp, where the production of CH_4 typically rose with temperature and the fraction of higher hydrocarbons were getting

smaller. CO_2 conversion is increasing with temperature, up to around 36% at 410°C, this trend seems to be universal with all catalyst. There is a possible link between this trend and the formation of *in-situ* generated iron carbides (Fe_5C_2) which are catalytic active species for CO_2 hydrogenation as compared to iron oxides. The presence of Fe_5C_2 was confirmed by XRD analysis of spent catalysts (Figure 36). And since blank FeO_x does not contain any copper, its conversion at 410°C is much lower than for the catalysts containing copper.

3%-Cu/FeO_x and 5%-Cu/FeO_x show a linear dependence of CO_2 conversion (Figure 40). These two were very similar after synthesis, with a similar particle size as opposed to blank FeO_x and 1%-Cu/FeO_x, it would be a possible explanation for this observation. The selectivity towards CO decreased in the second ramp. For 3%-Cu/FeO_x, in the first temperature ramp, there is noticeable an increase and then decrease in selectivity towards olefins and paraffins with the reaction temperature, the most optimal temperature range for these being 310-370°C. In the second ramp, with rising temperature, the trend of increasing selectivity towards C_2-C_4 olefins and decreasing selectivity towards C_2-C_4 paraffins is noticeable as well, however, it's not as drastic as when 1%-Cu/FeO_x was used. The selectivity towards CH_4 was increasing with the reaction temperature in the second ramp as well. The presence of Fe_5C_2 could explain this trend. 5%-Cu/FeO_x offers the best results for the production of C_5^+ hydrocarbons, however, selectivity towards CO is the highest out of all catalysts containing Cu NPs. The second ramp of 5%-Cu/FeO_x followed the same trend as with catalysts 1%-Cu/FeO_x and 3%-Cu/FeO_x regarding the selectivities towards paraffins and olefins. The presence of iron carbides (Fe_5C_2 and Fe_3C) was confirmed by STEM/HAADF (Figure 35) and XRD (Figure 36) analysis of the spent catalyst.

Figure 38 shows detailed CO_2 conversion and product selectivity during the first temperature ramp. Interesting to point out that at 250°C 1%-Cu/FeO_x showed no activity. At 280°C 1%-Cu/FeO_x still showed no activity and 3%-Cu/FeO_x along with 5%-Cu/FeO_x already show a large fraction of products. At 310°C we can already see the increased selectivity towards C_2-C_4 olefins with 1%-Cu/FeO_x, the selectivity to which seems to be decreasing with copper content. Blank FeO_x still shows a preference for CH_4. Product selectivity at 340°C shows the increase of selectivity towards CH_4 and CO with increasing copper content. Selectivity towards olefins is decreasing and towards paraffins slightly increasing with copper content. The production of higher C_5^+ hydrocarbons seems to be decreasing with copper content. At 370°C and 410°C, the selectivity trends are similar and it's interesting to point out that C_5^+ hydrocarbons are nearly not produced, only with blank FeO_x. As seen in Table 5, catalysts containing copper were developing iron carbides during

the catalysis, which could explain the difference in C_5^+ hydrocarbons selectivity at the higher temperatures between catalysts, spent blank FeO_x was proven to be a 100% magnetite, as opposed to copper-containing catalysts, which showed a various content of iron carbides. The high temperature can cause the breakdown of higher hydrocarbons as well.
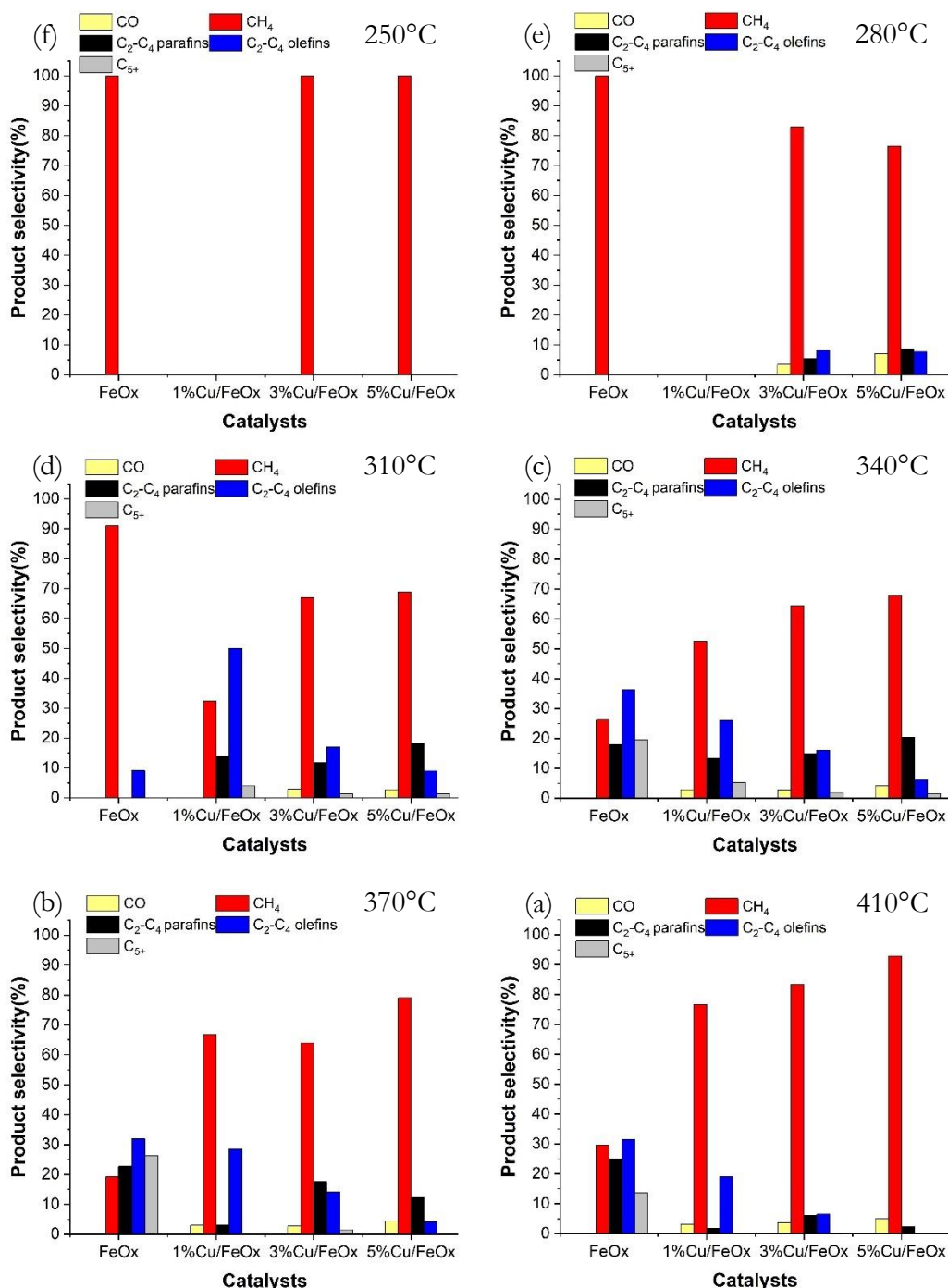
Figure 38. Product selectivity of the studied catalysts as the function of temperature during the first temperature ramp; (a) at 250°C, (b) at 280°C, (c) at 310°C, (d) at 340°C, (e) at 370°C and (f) at 410°C.
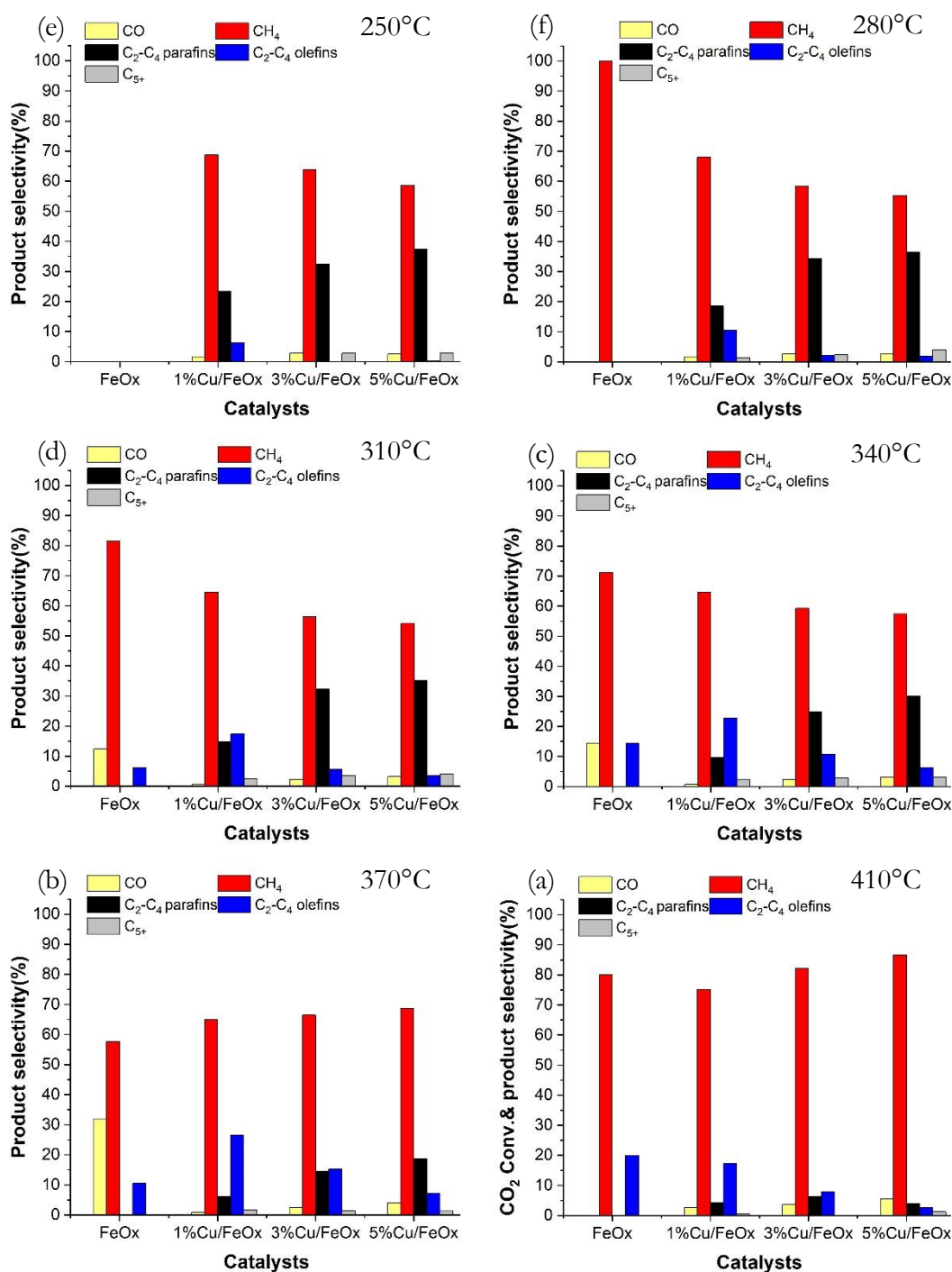
Figure 39. Product selectivity of the studied catalysts as the function of temperature during the first temperature ramp; (a) at 250°C, (b) at 280°C, (c) at 310°C, (d) at 340°C, (e) at 370°C and (f) at 410°C.

Figure 39 shows CO_2 conversion and product selectivity during the second temperature ramp. In the second ramp, there is a significant difference between blank FeO_x and 1%-Cu/FeO_x, then between 1%-Cu/FeO_x and 3%-Cu/FeO_x, 5%-Cu/FeO_x. Looking back at the particle size of the spent catalysts (as seen in Figure 6) we can see that there might be a correlation. This size difference in the spent catalysts could be explained by many factors, the most probably being the influence of copper content and the subsequent formation of

carbides and the overall composition of the spent catalysts (Table 5). In the second ramp, the catalysts seemed to be settled in their final form, containing magnetite and iron carbides and the changes during the second ramp seem to be reflecting their morphology. At 250°C, there is no activity with blank FeO_x, but 1%-Cu/FeO_x 3%-Cu/FeO_x and 5%-Cu/FeO_x show the decrease in selectivity towards CH_4 and C_2-C_4 olefins and increase in selectivity towards C_2-C_4 olefins C_5^+ hydrocarbons and CO. This trend can be recognised in the rest of the temperature ramp for copper-containing catalysts, except for the higher temperatures (370°C and 410°C) where the selectivity towards CH_4 seems to be increasing to the detriment of C_5^+ hydrocarbons. Meanwhile, blank FeO_x shows a 100% selectivity towards CH_4 at 280°C, and in the interval of 310-370°C show, a decrease in CH_4 selectivity and increase in CO selectivity, the production of C_2-C_4 olefins show a trend of the simple function of temperature.

Figure 40 compares the CO_2 conversion of our catalysts in the first and second temperature ramps. Conversion using FeO_x appears to be consistent in both temperature ramps. 1%-Cu/FeO_x, on the other hand, in the first ramp had a slower start, but with 340°C it converges with conversion in the second ramp, and at 410°C the catalyst has similar conversion to the following 3%-Cu/FeO_x and 5%-Cu/FeO_x in both ramps. With 3%-Cu/FeO_x and 5%-Cu/FeO_x, there is an obvious increase in conversion in the second ramp from 250°C, however, at 410°C both catalysts have similar conversion in both ramps.
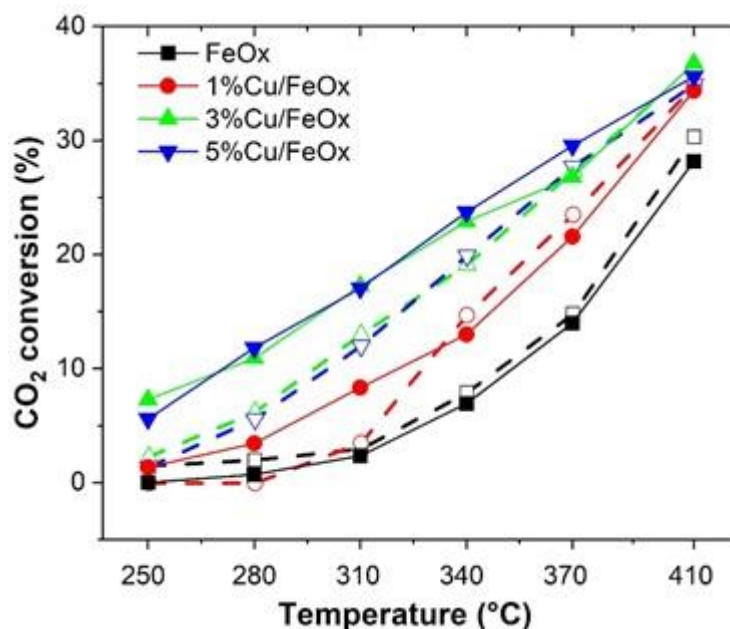
Figure 40. CO_2 conversion of different catalysts in the first (dashed line, hollow points) and second (full line, full points) temperature ramp of the catalysis.

6. Summary

By 2-step synthesis of iron oxide and following wet impregnation method, FeO_x catalysts were prepared with increasing Cu content (0%, 1%, 3% and 5%), named as (blank) FeO_x, 1%-Cu/FeO_x, 3%-Cu/FeO_x and 5%-Cu/FeO_x, respectively.

Prepared catalysts were characterised using typical techniques, such as transmission electron microscopy (TEM), scanning electron microscopy (SEM), high-resolution transmission spectroscopy (HRTEM) with high-angle annular dark-field scanning transmission electron microscopy (STEM/HAADF), energy-dispersive X-ray spectroscopy (EDX), powder X-ray diffraction (XRD), sorption of N_2 with Brunauer-Emmett-Teller (BET) model and X-ray photoelectron spectroscopy (XPS). The catalysts were characterised after being used in CO_2 hydrogenation, to study their changes during the reaction.

The catalytic activity was studied on CO_2 hydrogenation, performed in a Microactivity Reactor System, PID of Eng&Tech/Micromeritics having a quartz tube reactor of 320 mm in length and 12.7 mm diameter coupled. No pre-treatment was done on the catalysts before testing. The gas mixture introduced to the reactor contained CO_2, H_2 and He in a 1:5:4 ratio with a total flow of 25 mL/min. The temperature range of the reaction was 250 – 410°C in two consecutive temperature ramps, with product detection in 30°C intervals by gas chromatography.

The morphology of prepared catalysts was different, with FeO_x and 1%-Cu/FeO_x having the biggest apparent particles of iron oxide, as seen in SEM images, but have the largest specific surface area and therefore largest active surface, confirmed by BET. These two catalysts are porous, more so than 3%-Cu/FeO_x and 5%-Cu/FeO_x, which on SEM images look like fine wool, with their nanoneedle structures of iron oxide. 5%-Cu/FeO_x even has some spherical morphologies on the surface of iron oxide, most likely caused by etching of the surface with side products during preparation.

XRD analysis performed on fresh and spent catalysts reveal the reduction of initial mixtures of iron oxides and iron oxyhydroxide components of the catalysts into a mixture of iron oxides and iron carbides. It is debated that the presence of copper accelerates this transformation into carbides, as copper reduces, which affected the catalyst's performance. Namely the selectivity towards higher C_5^+ hydrocarbons.

After the first temperature ramp, the catalysts were transformed into their final form of iron carbides decorated with Cu NPs. This caused the selectivity towards products and CO_2 conversion to have a more predictable course, starting from the lowest temperatures. With increasing copper content, the production of methane (which was the most abundant product) decreased, the production of paraffins increased, the production of olefins decreased and the production of higher hydrocarbons decreased at each temperature step. At 410°C however, there was an observable increase in selectivity towards methane, as higher hydrocarbons tended to decompose. The selectivity towards CO stayed at comparable levels as selectivity towards higher hydrocarbons.

Overall, in this work, there were prepared highly active Cu/FeO_x catalysts with selective morphology, due to the influence of reactants and/or side products of the preparation reactions, which can be used for CO_2 hydrogenation. With further research, we can design a catalyst, with such a ratio of FeO_x and Cu NPs and tune the reaction temperature to shift the balance of the reaction towards the desired hydrocarbons.

7. Závěr

V této práci byly připraveny katalyzátory, dvou krokovou syntézou oxidu železnatého a následnou impregnací nanočástic mědi z roztoku. Katalyzátory byly připraveny se vzrůstajícím obsahem mědi (0%, 1%, 3% and 5%), označeny jako FeO_x (blank), 1%-Cu/FeO_x, 3%-Cu/FeO_x a 5%-Cu/FeO_x.

Připravené katalyzátory byly charakterizovány typickými technikami, jako je transmisní elektronová mikroskopie (TEM), skenovací elektronová mikroskopie (SEM), transmisní elektronová mikroskopie s vysokým rozlišením (HRTEM) a skenovací transmisní elektronová mikroskopie prstencového tmavého pole s vysokým úhlem (STEM/HAADF), energiově-disperzní rentgenová spektroskopie (EDX), prášková rentgenová difrakce (XRD), sorpce dusíku s modelem BET (Brunauer-Emmett-Teller) a rentgenová spektroskopie (XPS). Katalyzátory byly charakterizovány i po použití při CO_2 hydrogenaci, aby se mohly studovat změny během reakce.

Katalytická aktivita byla studována na hydrogenaci CO_2 prováděné v reaktorovém systému Mikroactivity, PID zařízení Eng&Tech/Micromeritics s křemenným trubičkovým reaktorem o délce 320 mm a průměru 12,7 mm. Katalyzátory nebyly před reakcí nijak upravovány. Směs plynů zavedená do reaktoru obsahovala CO_2, H_2 a He v poměru 1:5:4 s celkovým průtokem 25 ml/min. Teplotní rozsah reakce byl 250 – 410°C ve dvou po sobě jdoucích teplotních rampách, s detekcí produktu v intervalech 30°C pomocí plynové chromatografie.

Morfologie připravených katalyzátorů byla odlišná, přičemž FeO_x a 1%-Cu/FeO_x měly zdánlivě největší částice oxidu železitého, jak je vidět na SEM snímcích, ale měly největší specifickou plochu, a tudíž největší aktivní povrch, což bylo potvrzeno pomocí BET. Tyto dva katalyzátory jsou více porézní než 3%-Cu/FeO_x a 5%-Cu/FeO_x, které na SEM obrázcích vypadají jako jemná vlna se strukturou nano jehliček oxidu železitého. 5%-Cu/FeO_x má dokonce některé kulovité morfologie na povrchu oxidu železitého, nejspíše způsobené leptáním povrchu postranními produkty během přípravy.

Analýza XRD provedená na čerstvých a použitých katalyzátorech odhalila redukci počátečních směsí oxidů a hydroxidů železa na směs oxidů železa a karbidů železa. Diskutuje se o tom, že přítomnost mědi urychluje tuto přeměnu na karbidy, s probíhající redukcí mědi, což ovlivnilo výkon katalyzátoru. Jmenovitě selektivitu k vyšším C_5^+ uhlovodíkům.

Po první teplotní rampě byly katalyzátory přeměněny na konečnou podobu karbidů železa zdobených Cu NPs. To způsobilo, že selektivita k produktům a konverze CO_2 mají předvídatelnější průběh, počínaje nejnižšími teplotami. Se zvyšujícím se obsahem mědi klesala výroba metanu (který byl nejhojnějším produktem), rostla výroba parafinů, snižovala se výroba olefinů a při jednotlivých teplotních krocích klesala produkce C_5^+ uhlovodíků. Při 410 °C však došlo k pozorovatelnému zvýšení selektivity vůči metanu, jelikož vyšší uhlovodíky měly tendenci se rozkládat. Selektivita vůči CO zůstala na srovnatelné úrovni jako selektivita vůči vyšším uhlovodíkům.

Závěrem, v této práci byly připraveny vysoce aktivní Cu/FeO_x katalyzátory se selektivní morfologií, díky vlivu reaktantů a/nebo vedlejších produktů reakcí během přípravy, které mohou být použity pro hydrogenaci oxidu. S dalším výzkumem můžeme navrhnout katalyzátor s takovým poměrem FeO_x a Cu NPs a naladit reakční teplotu na posun rovnováhy reakce směrem k požadovaným uhlovodíkům.

8.   Reference

1.   Friedlingstein, P., et al., *Global Carbon Budget 2020.* Earth System Science Data, 2020. **12**(4): p. 3269-3340.
2.   Anderson, T.R., E. Hawkins, and P.D. Jones, *CO_2, the greenhouse effect and global warming: from the pioneering work of Arrhenius and Callendar to today's Earth System Models.* Endeavour, 2016. **40**(3): p. 178-187.
3.   Mac Dowell, N., et al., *The role of CO_2 capture and utilization in mitigating climate change.* Nature Climate Change, 2017. **7**(4): p. 243-249.
4.   Centi, G. and S. Perathoner, *Opportunities and prospects in the chemical recycling of carbon dioxide to fuels.* Catalysis Today, 2009. **148**(3): p. 191-205.
5.   Dupont , J., *Across the Board: Jairton Dupont.* ChemSusChem, 2015. **8**(4): p. 586-587.
6.   Peters, M., et al., *Chemical Technologies for Exploiting and Recycling Carbon Dioxide into the Value Chain.* ChemSusChem, 2011. **4**(9): p. 1216-1240.
7.   North, M., R. Pasquale, and C. Young, *Synthesis of cyclic carbonates from epoxides and CO_2.* Green Chemistry, 2010. **12**(9): p. 1514-1539.
8.   De, S., et al., *Advances in the Design of Heterogeneous Catalysts and Thermocatalytic Processes for CO_2 Utilization.* ACS Catalysis, 2020. **10**(23): p. 14147-14185.
9.   Ra, E.C., et al., *Recycling Carbon Dioxide through Catalytic Hydrogenation: Recent Key Developments and Perspectives.* ACS Catalysis, 2020. **10**(19): p. 11318-11345.
10. Valenti, G., et al., *Water-Mediated ElectroHydrogenation of CO_2 at Near-Equilibrium Potential by Carbon Nanotubes/Cerium Dioxide Nanohybrids.* ACS Applied Energy Materials, 2020. **3**(9): p. 8509-8518.
11. Choi, Y.H., et al., *Carbon dioxide Fischer-Tropsch synthesis: A new path to carbon-neutral fuels.* Applied Catalysis B: Environmental, 2017. **202**: p. 605-610.
12. Dorner, R.W., et al., *K and Mn doped iron-based CO_2 hydrogenation catalysts: Detection of $KAlH_4$ as part of the catalyst's active phase.* Applied Catalysis A: General, 2010. **373**(1-2): p. 112-121.
13. Dorner, R.W., et al., *C2-C5+ olefin production from CO_2 hydrogenation using ceria modified Fe/Mn/K catalysts.* Catalysis Communications, 2011. **15**(1): p. 88-92.
14. Centi, G., E.A. Quadrelli, and S. Perathoner, *Catalysis for CO_2 conversion: a key technology for rapid introduction of renewable energy in the value chain of chemical industries.* Energy & Environmental Science, 2013. **6**(6): p. 1711-1731.
15. Müller, K., L. Mokrushina, and W. Arlt, *Thermodynamic Constraints for the Utilization of CO_2.* Chemie Ingenieur Technik, 2014. **86**(4): p. 497-503.
16. Porosoff, M.D., B. Yan, and J.G. Chen, *Catalytic reduction of CO_2 by H_2 for synthesis of CO, methanol and hydrocarbons: challenges and opportunities.* Energy & Environmental Science, 2016. **9**(1): p. 62-73.
17. Wang, S.-G., et al., *Factors Controlling the Interaction of CO_2 with Transition Metal Surfaces.* The Journal of Physical Chemistry C, 2007. **111**(45): p. 16934-16940.
18. Wang, W., et al., *Fe–Cu Bimetallic Catalysts for Selective CO_2 Hydrogenation to Olefin-Rich C2+ Hydrocarbons.* Industrial & Engineering Chemistry Research, 2018. **57**(13): p. 4535-4542.
19. *catalysis,* in *IUPAC Compendium of Chemical Terminology.* 2009.
20. *catalyst,* in *IUPAC Compendium of Chemical Terminology.* 2009.
21. Deutschmann, O., et al., *Heterogeneous catalysis and solid catalysts. Ullmann's Encyclopedia of Industrial Chemistry, 2009.* Weinheim, Germany: Wiley-VCH Verlag GmbH & Co. KGaA.
22. Ertl, G., et al., *Handbook of Heterogeneous Catalysis.* 2008.
23. Snoeckx, R. and A. Bogaerts, *Plasma technology - a novel solution for CO_2 conversion?* Chem Soc Rev, 2017. **46**(19): p. 5805-5863.

24. Atkins, P.W. and J. De Paula, *Physical chemistry*. 1998, Oxford university press, Oxford UK.

25. Leofantia, G., et al., *Surface area and pore texture of catalysts*. Catalysis Today, 1998. **41**: p. 207-219.

26. Jr., G.E.B., et al., *Metal oxide surfaces and their interactions with aqueous solutions and microbial organisms*. Chem. Rev., 1999. **99**: p. 77-174.

27. Cornell, R.M. and U. Schwertmann, *The iron oxides: structure, properties, reactions, occurrences and uses*. 2003: John Wiley & Sons.

28. Kolasinski, K.W., *Surface science: foundations of catalysis and nanoscience*. 2012: John Wiley & Sons.

29. James, O.O., et al., *Reflections on the chemistry of the Fischer–Tropsch synthesis*. RSC Advances, 2012. **2**(19): p. 7347-7366.

30. Dlugokencky, E. and P. Tans. *Trends in Atmospheric Carbon Dioxide*. 2021 [cited 2021 16.05]; Available from: gml.noaa.gov/ccgg/trends/.

31. Aresta, M. and A. Dibenedetto, *Utilisation of CO2 as a chemical feedstock: opportunities and challenges*. Dalton Trans, 2007(28): p. 2975-92.

32. Rafiee, A., et al., *Trends in CO2 conversion and utilization: A review from process systems perspective*. Journal of Environmental Chemical Engineering, 2018. **6**(5): p. 5771-5794.

33. Rihko-Struckmann, L.K.P., A.; Hanke-Rauschenbach, R.; Sundmacher, K., *Assessment of Methanol Synthesis Utilizing Exhaust CO2 for Chemical Storage of Electrical Energy*. Ind. Eng. Chem. Res., 2010. **49**: p. 11073–11078.

34. Huang, C.-H. and C.-S. Tan, *A Review: CO2 Utilization*. Aerosol and Air Quality Research, 2014. **14**(2): p. 480-499.

35. Jia, J., et al., *Heterogeneous catalytic hydrogenation of CO2 by metal oxides: defect engineering - perfecting imperfection*. Chem Soc Rev, 2017. **46**(15): p. 4631-4644.

36. Wang, W., et al., *Recent advances in catalytic hydrogenation of carbon dioxide*. Chem Soc Rev, 2011. **40**(7): p. 3703-27.

37. Ma, J., et al., *A short review of catalysis for CO2 conversion*. Catalysis Today, 2009. **148**(3-4): p. 221-231.

38. Sternberg, A. and A. Bardow, *Life Cycle Assessment of Power-to-Gas: Syngas vs Methane*. ACS Sustainable Chemistry & Engineering, 2016. **4**(8): p. 4156-4165.

39. Razali, N.A.M., et al., *Heterogeneous catalysts for production of chemicals using carbon dioxide as raw material: A review*. Renewable and Sustainable Energy Reviews, 2012. **16**(7): p. 4951-4964.

40. Zhou, X., et al., *Shape selective plate-form Ga(2)O(3) with strong metal-support interaction to overlying Pd for hydrogenation of CO(2) to CH(3)OH*. Chem Commun (Camb), 2013. **49**(17): p. 1747-9.

41. Fidalgo, J., et al., *Versatile Rh- and Ir-Based Catalysts for CO2 Hydrogenation, Formic Acid Dehydrogenation, and Transfer Hydrogenation of Quinolines*. Inorg Chem, 2018. **57**(22): p. 14186-14198.

42. Qadir, M.I., et al., *Synergistic CO2 hydrogenation over bimetallic Ru/Ni nanoparticles in ionic liquids*. Applied Catalysis B: Environmental, 2019. **252**: p. 10-17.

43. Al-Dossary, M., et al., *Effect of Mn loading onto MnFeO nanocomposites for the CO2 hydrogenation reaction*. Applied Catalysis B: Environmental, 2015. **165**: p. 651-660.

44. Albrecht, M., et al., *Unexpectedly efficient CO2 hydrogenation to higher hydrocarbons over non-doped Fe2O3*. Applied Catalysis B: Environmental, 2017. **204**: p. 119-126.

45. Satthawong, R., et al., *Bimetallic Fe–Co catalysts for CO2 hydrogenation to higher hydrocarbons*. Journal of CO2 Utilization, 2013. **3-4**: p. 102-106.

46. Li, D., Ichikuni, N., Shimazu, S. and Uematsu, T., *Catalytic properties of sprayed Ru/Al2O3 and promoter effects of alkali metals in CO2 hydrogenation*. Applied Catalysis A: General, 1998. **172**(2): p. 351-358.

47.   Zhang, Y., Jacobs, G., Sparks, D., Dry, M. and Davis, B., *CO and CO2 hydrogenation study on supported cobalt Fischer–Tropsch synthesis catalysts.* Catalysis Today, 2002. **71**(3-4): p. 411-418.

48.   Calizzi, M., et al., *CO2 Hydrogenation over Unsupported Fe-Co Nanoalloy Catalysts.* Nanomaterials (Basel), 2020. **10**(7).

49.   Malaza, S.S.P. and B.C.E. Makhubela, *Direct and indirect CO2 hydrogenation catalyzed by Ir(III), Rh(III), Ru(II), and Os(II) half-sandwich complexes to generate formates and N,N-diethylformamide.* Journal of CO2 Utilization, 2020. **39**.

50.   Weatherbee, G., *Hydrogenation of CO2 on group VIII metals IV. Specific activities and selectivities of silica-supported Co, Fe, and Ru.* Journal of Catalysis, 1984. **87**(2): p. 352-362.

51.   Liang, B., et al., *Mn decorated Na/Fe catalysts for CO2 hydrogenation to light olefins.* Catalysis Science & Technology, 2019. **9**(2): p. 456-464.

52.   Perkas, N., et al., *Sonochemical deposition of magnetite on silver nanocrystals.* Ultrason Sonochem, 2009. **16**(1): p. 132-5.

53.   Furnival, T., et al., *Anomalous diffusion of single metal atoms on a graphene oxide support.* Chemical Physics Letters, 2017. **683**: p. 370-374.

54.   Datta, K.J., et al., *Micro–mesoporous iron oxides with record efficiency for the decomposition of hydrogen peroxide: morphology driven catalysis for the degradation of organic contaminants.* Journal of Materials Chemistry A, 2016. **4**(2): p. 596-604.

55.   Lee, S., et al., *Subnanometer cobalt oxide clusters as selective low temperature oxidative dehydrogenation catalysts.* Nat Commun, 2019. **10**(1): p. 954.

56.   Lee, S., et al., *Support-dependent Performance of Size-selected Subnanometer Cobalt Cluster-based Catalysts in the Dehydrogenation of Cyclohexene.* ChemCatChem, 2012. **4**(10): p. 1632-1637.

57.   Fang, X., et al., *Tetragonal zirconia based ternary ZnO-ZrO2-MOx solid solution catalysts for highly selective conversion of CO2 to methanol at High reaction temperature.* Journal of Industrial and Engineering Chemistry, 2020. **88**: p. 268-277.

58.   Qadir, M.I., et al., *Selective Carbon Dioxide Hydrogenation Driven by Ferromagnetic RuFe Nanoparticles in Ionic Liquids.* ACS Catalysis, 2018. **8**(2): p. 1621-1627.

59.   Millet, M.-M., et al., *Ni Single Atom Catalysts for CO2 Activation.* Journal of the American Chemical Society, 2019. **141**(6): p. 2451-2461.

60.   Dorner, R.W., et al., *Influence of Gas Feed Composition and Pressure on the Catalytic Conversion of CO2 to Hydrocarbons Using a Traditional Cobalt-Based Fischer−Tropsch Catalyst.* Energy & Fuels, 2009. **23**(8): p. 4190-4195.

61.   Gnanamani, M.K., et al., *Fischer-Tropsch synthesis: Effect of pretreatment conditions of cobalt on activity and selectivity for hydrogenation of carbon dioxide.* Applied Catalysis A: General, 2015. **499**: p. 39-46.

62.   Sun, Q., et al., *In2O3 as a promising catalyst for CO2 utilization: A case study with reverse water gas shift over In2O3.* Greenhouse Gases: Science and Technology, 2014. **4**(1): p. 140-144.

63.   Chen, W.-H., *CO2 conversion for syngas production in methane catalytic partial oxidation.* Journal of CO2 Utilization, 2014. **5**: p. 1-9.

64.   Gnanamani, M.K., et al., *Hydrogenation of Carbon Dioxide over Co–Fe Bimetallic Catalysts.* ACS Catalysis, 2016. **6**(2): p. 913-927.

65.   Zhu, Y., et al., *Catalytic Conversion of Carbon Dioxide to Methane on Ruthenium–Cobalt Bimetallic Nanocatalysts and Correlation between Surface Chemistry of Catalysts under Reaction Conditions and Catalytic Performances.* ACS Catalysis, 2012. **2**(11): p. 2403-2408.

66.   Duyar, M.S., et al., *Low-pressure methanol synthesis from CO2 over metal-promoted Ni-Ga intermetallic catalysts.* Journal of CO2 Utilization, 2020. **39**.

67.   Zhang, Y., et al., *Tuning selectivity of CO2 hydrogenation by modulating the strong metal–support interaction over Ir/TiO2 catalysts.* Green Chemistry, 2020. **22**(20): p. 6855-6861.

68.	Li, X., et al., *Controlling CO2 Hydrogenation Selectivity by Metal-Supported Electron Transfer.* Angewandte Chemie International Edition, 2020. **59**(45): p. 19983-19989.

69.	Riedel, T., Shulz, H., Schaub, G., Jun, K.-W., *Fischer–Tropsch on iron with H2/CO and H2/CO2 as synthesis gases: the episodes of formation of the Fischer–Tropsch regime and construction of the catalyst.* Topics in Catalysis, 2003. **26**(1-4): p. 41-54.

70.	Hwang, J.S., K.-W. Jun, and K.-W. Lee, *Deactivation and regeneration of Fe-K/alumina catalyst in CO2 hydrogenation.* Applied Catalysis A: General, 2001. **208**(1): p. 217-222.

71.	Hong, J.-S., et al., *Deactivation study on a coprecipitated Fe-Cu-K-Al catalyst in CO2 hydrogenation.* Applied Catalysis A: General, 2001. **218**(1): p. 53-59.

72.	Pérez-Alonso, F.J., et al., *Carbon dioxide hydrogenation over Fe–Ce catalysts.* Catalysis Communications, 2008. **9**(9): p. 1945-1948.

73.	Rodemerck, U., et al., *Catalyst Development for CO2 Hydrogenation to Fuels.* ChemCatChem, 2013. **5**(7): p. 1948-1955.

74.	Aitbekova, A., et al., *Engineering of Ruthenium–Iron Oxide Colloidal Heterostructures: Improved Yields in CO2 Hydrogenation to Hydrocarbons.* Angewandte Chemie International Edition, 2019. **58**(48): p. 17451-17457.

75.	Liang, B., et al., *Effect of Na Promoter on Fe-Based Catalyst for CO2 Hydrogenation to Alkenes.* ACS Sustainable Chemistry & Engineering, 2019. **7**(1): p. 925-932.

76.	Wei, J., et al., *Catalytic Hydrogenation of CO2 to Isoparaffins over Fe-Based Multifunctional Catalysts.* ACS Catalysis, 2018. **8**(11): p. 9958-9967.

77.	Choi, Y.H., et al., *Sodium-Containing Spinel Zinc Ferrite as a Catalyst Precursor for the Selective Synthesis of Liquid Hydrocarbon Fuels.* ChemSusChem, 2017. **10**(23): p. 4764-4770.

78.	Kim, K.Y., et al., *Cobalt Ferrite Nanoparticles to Form a Catalytic Co–Fe Alloy Carbide Phase for Selective CO2 Hydrogenation to Light Olefins.* ACS Catalysis, 2020: p. 8660-8671.

79.	Ronda-Lloret, M., G. Rothenberg, and N.R. Shiju, *A Critical Look at Direct Catalytic Hydrogenation of Carbon Dioxide to Olefins.* ChemSusChem, 2019. **12**(17): p. 3896-3914.

80.	Bradley, M.J., et al., *The Effect of Copper Addition on the Activity and Stability of Iron-Based CO2 Hydrogenation Catalysts.* Molecules, 2017. **22**(9): p. 1579.

81.	Previtali, D., et al., *Low pressure conversion of CO2 to methanol over Cu/Zn/Al catalysts. The effect of Mg, Ca and Sr as basic promoters.* Fuel, 2020. **274**.

82.	Halder, A., et al., *Highly efficient Cu-decorated iron oxide nanocatalyst for low pressure CO2 conversion.* Applied Catalysis B: Environmental, 2018. **225**: p. 128-138.

83.	Zhang, P., et al., *Urea-derived Cu/ZnO catalyst being dried by supercritical CO2 for low-temperature methanol synthesis.* Fuel, 2020. **268**.

84.	Xiong, S., et al., *Hydrogenation of CO2 to methanol over Cu/ZnCr catalyst.* Fuel, 2019. **256**.

85.	Dong, X., et al., *CO2 hydrogenation to methanol over Cu/ZnO/ZrO2 catalysts prepared by precipitation-reduction method.* Applied Catalysis B: Environmental, 2016. **191**: p. 8-17.

86.	Wang, G., et al., *Enhanced performance of the CuO-ZnO-ZrO2 catalyst for CO2 hydrogenation to methanol by WO3 modification.* Applied Surface Science, 2018. **456**: p. 403-409.

87.	Li, S., et al., *A highly active and selective mesostructured Cu/AlCeO catalyst for CO2 hydrogenation to methanol.* Applied Catalysis A: General, 2019. **571**: p. 51-60.

88.	Sedighi, M. and M. Mohammadi, *CO2 hydrogenation to light olefins over Cu-CeO2/SAPO-34 catalysts: Product distribution and optimization.* Journal of CO2 Utilization, 2020. **35**: p. 236-244.

89.	Gao, P., et al., *Cu/Zn/Al/Zr catalysts via phase-pure hydrotalcite-like compounds for methanol synthesis from carbon dioxide.* Journal of CO2 Utilization, 2015. **11**: p. 41-48.

90.	Yang, B., et al., *Copper Cluster Size Effect in Methanol Synthesis from CO2.* The Journal of Physical Chemistry C, 2017. **121**(19): p. 10406-10412.

91.   Dasireddy, V.D.B.C. and B. Likozar, *The role of copper oxidation state in Cu/ZnO/Al2O3 catalysts in CO2 hydrogenation and methanol productivity.* Renewable Energy, 2019. **140**: p. 452-460.

92.   Liu, C., et al., *Carbon Dioxide Conversion to Methanol over Size-Selected Cu4 Clusters at Low Pressures.* J Am Chem Soc, 2015. **137**(27): p. 8676-9.

93.   Chernyak, S.A., et al., *Sintered Fe/CNT framework catalysts for CO2 hydrogenation into hydrocarbons.* Carbon, 2020.

94.   Jiang, F., et al., *Hydrogenation of CO2 into hydrocarbons: enhanced catalytic activity over Fe-based Fischer–Tropsch catalysts.* Catalysis Science & Technology, 2018. **8**(16): p. 4097-4107.

95.   Kirchner, J., Z. Baysal, and S. Kureti, *Activity and Structural Changes of Fe-based Catalysts during CO2 Hydrogenation towards CH4 – A Mini Review.* ChemCatChem, 2020. **12**(4): p. 981-988.

96.   Zimmermann, H. and R. Walzl, *Ethylene*, in *Ullmann's encyclopedia of industrial chemistry.* 2009, Wiley-VCH Verlag GmbH & Co. KGaA: Weinheim.

97.   Amghizar, I., et al., *New Trends in Olefin Production.* Engineering, 2017. **3**(2): p. 171-178.

98.   Grabowski, R., *Kinetics of Oxidative Dehydrogenation of C2-C3 Alkanes on Oxide Catalysts.* Catalysis Reviews, 2006. **48**(2): p. 199-268.

99.   Gärtner, C.A., A.C. van Veen, and J.A. Lercher, *Oxidative Dehydrogenation of Ethane: Common Principles and Mechanistic Aspects.* ChemCatChem, 2013. **5**(11): p. 3196-3217.

100.   Shaobin Wang, K.M., T. Hayakawa, S. Hamakawa, K. Suzuki, *Dehydrogenation of ethane with carbon dioxide over supported chromium oxide catalysts.* Applied Catalysis A: General, 2000. **196**: p. 1-8.

101.   Bharadwaj, S.S. and L.D. Schmidt, *Platinum-tin and platinum-copper catalysts for autothermal oxidative dehydrogenation of ethane to ethylene.* Catalysis Letters, 1996. **38**: p. 181-188.

102.   Sattler, J.J., et al., *Catalytic dehydrogenation of light alkanes on metals and metal oxides.* Chem Rev, 2014. **114**(20): p. 10613-53.

103.   Nawaz, Z., *Light alkane dehydrogenation to light olefin technologies: a comprehensive review.* Reviews in Chemical Engineering, 2015. **31**(5).

104.   Xu, Q. and M. Chandra, *Catalytic activities of non-noble metals for hydrogen generation from aqueous ammonia–borane at room temperature.* Journal of Power Sources, 2006. **163**(1): p. 364-370.

105.   Chen, M., et al., *Study in support effect of In2O3/MOx (M=Al, Si, Zr) catalysts for dehydrogenation of propane in the presence of CO2.* Applied Catalysis A: General, 2011. **407**(1-2): p. 20-28.

106.   Shao, C.-T., et al., *Catalytic performance of gallium oxide based-catalysts for the propane dehydrogenation reaction: effects of support and loading amount.* RSC Advances, 2017. **7**(8): p. 4710-4723.

107.   Ren, Y., et al., *Ga2O3/HZSM-48 for dehydrogenation of propane: Effect of acidity and pore geometry of support.* Journal of Industrial and Engineering Chemistry, 2012. **18**(2): p. 731-736.

108.   Klisińska, A., et al., *Effect of additives on properties of V2O5/SiO2 and V2O5/MgO catalysts.* Applied Catalysis A: General, 2006. **309**(1): p. 17-27.

109.   Botella, P., et al., *Selective oxidative dehydrogenation of ethane over MoVSbO mixed oxide catalysts.* Applied Catalysis A: General, 2006. **298**: p. 16-23.

110.   Heracleous, E., et al., *Oxidative dehydrogenation of ethane and propane over vanadia and molybdena supported catalysts.* Journal of Molecular Catalysis A: Chemical, 2005. **232**(1-2): p. 29-39.

111.   Botella, P., *Selective oxidative dehydrogenation of ethane on MoVTeNbO mixed metal oxide catalysts.* Journal of Catalysis, 2004. **225**(2): p. 428-438.

112. Bars, J.L., et al., *Active Sites of V2O5/γ-Al2O3 Catalysts in the Oxidative Dehydrogenation of Ethane.* Journal of Catalysis, 1996. **162**: p. 250-259.

113. Agafonov, Y.A., N.A. Gaidai, and A.L. Lapidus, *Influence of the preparation conditions for catalysts CrOx/SiO2 on their efficiency in propane dehydrogenation in the presence CO2.* Russian Chemical Bulletin, International Edition, 2014. **63**(2): p. 381—388.

114. Zaccheria, F., et al., *Synthetic scope of alcohol transfer dehydrogenation catalyzed by Cu/Al2O3: a new metallic catalyst with unusual selectivity.* Chemistry, 2006. **12**(24): p. 6426-31.

115. Yu-Ming Lin, I.W., Chuin-Tih Yeh, *Activity and Stability of a Copper(I1) Oxide- Zinc(H) Oxide Catalyst for Oxidative Dehydrogenation of Cyclohexanol to Cyclohexanone.* Applied Catalysis, 1988. **41**: p. 53-63.

116. Sun, D., et al., *Selective hydrogenation of γ-valerolactone to 2-methyltetrahydrofuran over Cu/Al2O3 catalyst.* Applied Catalysis A: General, 2020. **590**.

117. Sobczak, I. and Ł. Wolski, *Au–Cu on Nb2O5 and Nb/MCF supports – Surface properties and catalytic activity in glycerol and methanol oxidation.* Catalysis Today, 2015. **254**: p. 72-82.

118. Shan, J., et al., *Water co-catalyzed selective dehydrogenation of methanol to formaldehyde and hydrogen.* Surface Science, 2016. **650**: p. 121-129.

119. Shan, J., et al., *NiCu single atom alloys catalyze the C H bond activation in the selective non-oxidative ethanol dehydrogenation reaction.* Applied Catalysis B: Environmental, 2018. **226**: p. 534-543.

120. Shan, J., et al., *Selective non-oxidative dehydrogenation of ethanol to acetaldehyde and hydrogen on highly dilute NiCu alloys.* Applied Catalysis B: Environmental, 2017. **205**: p. 541-550.

121. Poreddy, R., C. Engelbrekt, and A. Riisager, *Copper oxide as efficient catalyst for oxidative dehydrogenation of alcohols with air.* Catalysis Science & Technology, 2015. **5**(4): p. 2467-2477.

122. Marcinkowski, M.D., Darby, M. T., Liu, J., Wimble, J. M., Lucci, F. R., Lee, S., Michaelides, A., Flytzani-Stephanopoulos, M., Stamatakis, M., Sykes, E. Ch. H., *Pt-Cu single-atom alloys as coke-resistant catalysts for efficient C–H activation.* Nature Chemistry, 2018. **10**: p. 325-332.

123. Maniecki, T.P., et al., *Bimetallic Au–Cu, Ag–Cu/CrAl3O6 Catalysts for Methanol Synthesis.* Catalysis Letters, 2009. **130**(3-4): p. 481-488.

124. K. Yamamoto, Y.G.C., F.G. Buono, *Oxidative dehydrogenation of dihydropyrimidinones and dihydropyrimidines.* Organic Letters, 2005. **7**(21): p. 4673-4676.

125. Chen, L., et al., *Cu/SiO2 catalysts prepared by the ammonia-evaporation method: Texture, structure, and catalytic performance in hydrogenation of dimethyl oxalate to ethylene glycol.* Journal of Catalysis, 2008. **257**(1): p. 172-180.

126. Hu, Z. and F.M. Kerton, *Simple copper/TEMPO catalyzed aerobic dehydrogenation of benzylic amines and anilines.* Org Biomol Chem, 2012. **10**(8): p. 1618-24.

127. He, H., C. Zhang, and Y. Yu, *A comparative study of Ag/Al2O3 and Cu/Al2O3 catalysts for the selective catalytic reduction of NO by C3H6.* Catalysis Today, 2004. **90**(3-4): p. 191-197.

128. Han, Z., et al., *Propane dehydrogenation over Pt-Cu bimetallic catalysts: the nature of coke deposition and the role of copper.* Nanoscale, 2014. **6**(17): p. 10000-8.

129. Hamlyn, R., et al., *Morphology and chemical behavior of model CsOx/Cu2O/Cu(111) nanocatalysts for methanol synthesis: Reaction with CO2 and H2.* J Chem Phys, 2020. **152**(4): p. 044701.

130. Halder, A., et al., *Oxidative Dehydrogenation of Cyclohexane by Cu vs Pd Clusters: Selectivity Control by Specific Cluster Dynamics.* ChemCatChem, 2020. **12**(5): p. 1307-1315.

131. Conde, A., et al., *Introducing copper as catalyst for oxidative alkane dehydrogenation.* J Am Chem Soc, 2013. **135**(10): p. 3887-96.

132. Cao, X., Y. Ji, and Y. Luo, *Dehydrogenation of Propane to Propylene by a Pd/Cu Single-Atom Catalyst: Insight from First-Principles Calculations.* The Journal of Physical Chemistry C, 2014. **119**(2): p. 1016-1023.

133. C. Marchal-Roch, R.B., J.F. Moisan, A. Tézé and G. Hervé, *Oxidative dehydrogenation of isobutyric acid: characterization and modeling of vanadium containing polyoxometalate catalysts.* Topics in Catalysis, 1996. **3**: p. 407-419.

134. B.B. Bardin, R.J.D., *Characterization of copper and vanadium containing heteropolyacid catalysts for oxidative dehydrogenation of propane.* applied Catalysis A: General, 1999. **185**: p. 283-292.

135. Avik Halder, M.-A.H., Huanchen Zhai, Bing Yang, Michael J. Pellin, Sönke Seifert, Anastassia N. Alexandrova, Stefan Vajda, *Oxidative Dehydrogenation of Cyclohexane by Cu vs Pd Clusters: Selectivity Control by Specific Cluster Dynamics - suplementary information.* ChemCatChem, 2020. **12**(5): p. 1307-1315.

136. Zaccheria, F., et al., *Heterogeneous selective catalytic hydrogenation of aryl ketones to alcohols without additives.* Tetrahedron Letters, 2005. **46**(21): p. 3695-3697.

137. Zboril, R., et al., *Structural, magnetic and size transformations induced by isothermal treatment of ferrous oxalate dihydrate in static air conditions.* physica status solidi (c), 2004. **1**(12): p. 3583-3588.

138. Bani-Hani, M., R. Abd-Allah, and L. El-Khouri, *Archeaometallurgical finds from Barsinia, Northern Jordan: Microstructural characterization and conservation treatment.* Journal of Cultural Heritage, 2012. **13**(3): p. 314-325.

139. Irfan, M.A., et al., *Porosity reduction and mechanical properties improvement in die cast engine blocks.* Materials Science and Engineering: A, 2012. **535**: p. 108-114.

140. Sayed, F.N. and V. Polshettiwar, *Facile and sustainable synthesis of shaped iron oxide nanoparticles: effect of iron precursor salts on the shapes of iron oxides.* Sci Rep, 2015. **5**: p. 9733.

141. Khayatian, G., et al., *Spectrophotometric Determination of Trace Amounts of Uranium(VI) using Modified Magnetic Iron Oxide Nanoparticles in Environmental and Biological Samples.* Journal of the Brazilian Chemical Society, 2013.

142. Adhikari, M., et al., *Synthesis of Magnetite Nanorods from the Reduction of Iron Oxy-Hydroxide with Hydrazine.* ACS Omega, 2020. **5**(35): p. 22440-22448.

143. Cheng, G. and A.R. Hight Walker, *Transmission electron microscopy characterization of colloidal copper nanoparticles and their chemical reactivity.* Analytical and Bioanalytical Chemistry, 2010. **396**(3): p. 1057-1069.

144. Zhu, D., et al., *Intriguingly high thermal conductivity increment for CuO nanowires contained nanofluids with low viscosity.* Sci Rep, 2018. **8**(1): p. 5282.

145. Halder, A., et al., *CO2 Methanation on Cu-Cluster Decorated Zirconia Supports with Different Morphology: A Combined Experimental In Situ GIXANES/GISAXS, Ex Situ XPS and Theoretical DFT Study.* ACS Catalysis, 2021: p. 6210-6224.

146. Pauly, N., S. Tougaard, and F. Yubero, *Determination of the Cu 2p primary excitation spectra for Cu, Cu2O and CuO.* Surface Science, 2014. **620**: p. 17-22.

147. Kim, E., et al., *Etching-Assisted Crumpled Graphene Wrapped Spiky Iron Oxide Particles for High-Performance Li-Ion Hybrid Supercapacitor.* Small, 2018. **14**(16): p. e1704209.

148. de Smit, E. and B.M. Weckhuysen, *The renaissance of iron-based Fischer–Tropsch synthesis: on the multifaceted catalyst deactivation behaviour.* Chemical Society Reviews, 2008. **37**(12): p. 2758-2781.

149. Pendyala, V.R.R., et al., *Fischer–Tropsch Synthesis: Morphology, Phase Transformation, and Carbon-Layer Growth of Iron-Based Catalysts.* ChemCatChem, 2014. **6**(7): p. 1952-1960.